Quaternary Science Reviews 300 (2023) 107868

Contents lists available at ScienceDirect

Quaternary Science Reviews

journal homepage: www.elsevier.com/locate/quascirev

Within-region replication of late Holocene relative sea-level change: An example from southern New England, United States

Rachel B. Stearns [a], Simon E. Engelhart [b, *], Andrew C. Kemp [c], Troy D. Hill [d, e], Matthew J. Brain [b], D. Reide Corbett [f]

[a] Department of Geosciences, University of Rhode Island, Kingston, RI, 02881, USA
[b] Department of Geography, Durham University, Durham, DH1 3LE, UK
[c] Department of Earth and Climate Sciences, Tufts University, Medford, MA, 02155, USA
[d] South Florida Natural Resources Center, National Park Service, Boynton Beach, FL, 33473, USA
[e] Region 8, U.S. Environmental Protection Agency, Denver, CO, 80202, USA
[f] Coastal Studies Institute, East Carolina University, Wanchese, NC, 27981, USA

ARTICLE INFO

Article history:
Received 9 September 2022
Received in revised form
4 November 2022
Accepted 5 November 2022
Available online xxx

Handling Editor: Dr I Hendy

Keywords:
Holocene
Bayesian
Sea level changes
North Atlantic
Micropaleontology
Foraminifers
Hotspot
Organic geochemistry
Salt marsh
Data treatment
Data analysis
Geomorphology
Coastal

ABSTRACT

Tide-gauge measurements in the western North Atlantic Ocean show coherent, multi-decadal relative sea-level (RSL) trends across multiple spatial scales. Proxy reconstructions developed from salt-marsh sediment can extend this instrumental record. However, the degree of coherence in proxy reconstructions is underexamined through within-region replication. To explore within-region replication, we developed a new RSL reconstruction from Fox Hill Marsh, Rhode Island to complement similar records at nearby sites. We established the elevation of former sea level from assemblages of foraminifera and bulk-sediment $\delta^{13}C$ values using a Bayesian transfer function. We employed radiocarbon dating and recognition of pollution horizons to construct a core chronology. Since ~1200 BCE, RSL rose by ~3.7 m at Fox Hill Marsh. After correction for glacial isostatic adjustment, application of a statistical model intended to quantify (multi-) century-scale trends showed that the fastest rate of rise in at least the past 3000 years was 1.71 ± 0.84 mm/yr (95% credible interval) in 2020 CE. This result replicates regional tide-gauge measurements and other proxy reconstructions. Using an alternative statistical model constructed to identify sub-centennial sea-level changes, we examined if there was a hotspot of 18th century rise in the northeastern United States and found no spatially-coherent trend (i.e., occurring at all or most sites). This lack of replication indicates that accelerated rise during the 18th century is likely local (site-specific) in scale, or an artifact of individual reconstructions. Continued efforts to replicate RSL reconstructions will increase confidence in the accuracy of records and their subsequent interpretation.

1. Introduction

Relative sea-level (RSL) reconstructions contextualize modern rates of rise and projections of future sea-level change with its associated risks to ecosystems, infrastructure, and human coastal populations (e.g., Bittermann et al., 2013; Gehrels et al., 2011; Strauss et al., 2012). The unique position of RSL in time and space arises from the interplay of multiple physical processes (e.g., Clark et al., 1978; Milne et al., 2009). Examining commonalities and differences among RSL records across space and through time provides an opportunity to recognize and quantify the contributions from specific physical processes. For example, 20th century RSL changes measured by tide gauges along the Atlantic coast of North America are used to evaluate ongoing glacio-isostatic adjustment (GIA; Peltier, 1996), decadal-scale variability in ocean circulation (McCarthy et al., 2015), annual changes in wind fields and atmospheric pressure (Piecuch et al., 2016), and the role of river discharge (Piecuch et al., 2018a). However, the limited duration of tide-gauge RSL measurements (and to a lesser extent in eastern North America than elsewhere, their geographic distribution) hinders efforts to evaluate the global, regional, and local drivers of RSL change on longer timescales and during earlier (pre-

* Corresponding author.
E-mail address: simon.e.engelhart@durham.ac.uk (S.E. Engelhart).

https://doi.org/10.1016/j.quascirev.2022.107868

anthropogenic) periods. Fortunately, late Holocene (defined here informally as the past ~3000 years) RSL changes are recorded by proxies preserved in the sedimentary record beneath modern-day salt marshes (e.g., Gehrels et al., 2005; Gerlach et al., 2017; Kemp et al., 2018b). However, identifying the physical origins of spatio-temporal variability in RSL requires replication of proxy reconstructions over spatial scales appropriate to the posited causal mechanisms (Gehrels et al., 2020).

Evaluating the relative importance of local- and regional-scale processes should be underpinned by comparison of RSL reconstructions with similar resolution and treatment of uncertainty from multiple sites within a region. RSL trends are often quantified using statistical models to make objective assessments with appropriate consideration of temporal and vertical uncertainty (Ashe et al., 2019). However, different models are rarely applied to datasets to understand if results are sensitive to model choice. It is therefore necessary to evaluate if, how, and why statistical models applied to single records and networks of discrete RSL reconstructions may generate (dis)similar sea-level histories from common input data. Regions with a high density of RSL reconstructions are the most suitable for examining the reproducibility of RSL trends and to weigh the likelihood that reconstructed trends are local (site-specific), or regional in scale (Ashe et al., 2019; Kemp et al., 2018b). The region with the greatest concentration of late Holocene RSL records is the northeastern United States and Canadian Maritimes, but even here additional records of comparable resolution and quality are needed to draw robust conclusions about local and regional-scale drivers of RSL change (Gehrels et al., 2020).

To address these issues for improving our understanding of the driving mechanisms and causal factors of late Holocene RSL changes, we produced a new reconstruction spanning the past ~3000 years using foraminifera and stable carbon isotopes preserved in a core of dated salt-marsh peat from Fox Hill Marsh in Rhode Island. We leveraged the new RSL reconstruction, along with the increasingly dense network of comparable records, to examine the replicability of RSL histories across spatial and temporal scales using two statistical models.

2. Study area

We investigated lower Narragansett Bay, Rhode Island for three reasons. Firstly, southern New England has a relatively high density of near-continuous late Holocene RSL reconstructions (Fig. 1A), which makes it an appropriate location for exploring within-region replication. Secondly, vertical uncertainties in RSL reconstructions have been shown to be correlated with tidal range (Barlow et al., 2013) and the modest (0.9–1.2 m) great diurnal tidal ranges (mean lower low water, MLLW to mean higher high water, MHHW) of lower Narragansett Bay offer an opportunity to increase the precision of late Holocene RSL reconstructions in southern New England (e.g., Kemp et al., 2015 studied East River where great diurnal tidal range is 1.75 m; Fig. 1). Thirdly, sites within the bay contain thick accumulations of salt-marsh peat that span ~3000 years (Donnelly and Bertness, 2001, Fig. 1B) and are suitable for extending near-continuous RSL reconstructions from the region (e.g., Gehrels et al., 2020 provided a ~600 year record from Barn Island; Fig. 1).

Narragansett Bay was sculpted by the Laurentide Ice Sheet, which retreated from southern Rhode Island by ~20,000 years BP (Oakley and Boothroyd, 2013). Subsequently, marine water transgressed Narragansett Bay by ~7,100 years BP (Peck and McMaster, 1991). Today, Narragansett Bay (Fig. 1B), including the islands within it, has 412 km of coastline, a mean depth of 8 m, a maximum depth of 56 m, and an average salinity that ranges from 24 in the upper bay to 32 towards the ocean. The tide gauge at Newport (Fig. 1) measured 20th century RSL rise at 2.86 ± 0.73 mm/yr, of which 1.06 ± 0.55 mm/yr is attributed to ongoing GIA (Piecuch et al., 2018b; 95% credible interval).

After exploratory coring at sites throughout Narragansett Bay, we selected Fox Hill Marsh because it preserves thick sequences of high salt-marsh peat with abundant plant macrofossils and is conveniently located ~1 km from the West Jamestown tide gauge (NOAA station number 8453742; Fig. 1B) that provides local tidal datums. Great diurnal tidal range at the site is 1.17 m. Unvegetated tidal flats (comprising inorganic silt and clay) transition directly to the high salt-marsh platform at an eroding and pronounced marsh edge; this geomorphology is characteristic of many salt marshes in the region. The distribution of C_4 and C_3 salt-marsh grasses at Fox Hill Marsh is similar to those documented elsewhere in Narragansett Bay (Crain et al., 2008; Wigand et al., 2003; Wozniak et al., 2006) and more widely in southern New England and the mid-Atlantic (e.g., Bertness, 1991; Niering and Warren, 1980; Nixon, 1982; Redfield, 1972). The peat-forming, high salt-marsh platform exists from approximately mean high water (MHW) to MHHW and is dominated by *Spartina patens* and *Distichlis spicata*, which both utilize the C_4 photosynthetic pathway. On the seaward edge of the platform some stands of *Spartina alterniflora* (C_4) are found and patches of *Salicornia virginica* (C_3) exist on the platform. The brackish, transitional marsh above MHHW is vegetated only by C_3 species (*Juncus gerardii*, *Schoenoplectus* spp., *Aster tenuifolius*, *Iva fructescens*, *Phragmites australis*, and *Typha* spp.). Above the reach of marine water is a freshwater, upland community comprised of C_3 species.

3. Methods

3.1. Sea-level proxies

3.1.1. Foraminifera

Foraminifera are sea-level proxies because they form distinctive assemblages that occupy salt-marsh surfaces at particular tidal elevations in response to environmental variables that are controlled by the frequency and duration of inundation, which is well approximated by elevation (e.g., Edwards and Wright, 2015; Scott and Medioli, 1978). Salt-marsh foraminifera are used to reconstruct paleomarsh elevation (PME) through reasoning by analogy, where the observed relationship between foraminifera and tidal elevation on modern salt marshes is the basis for interpreting analogous assemblages preserved in core material (e.g., Gehrels et al., 2005; Kemp et al., 2015). This approach requires a modern training set that can be local (usually specific to the site being investigated, i.e., Fox Hill Marsh), or regional in scale (drawn from multiple sites to capture greater variability in environmental factors and species response, while also providing a greater diversity of modern analogs).

We collected surface (0–1 cm depth) sediment samples along four transects at Fox Hill Marsh (Fig. 1C) to quantify the local relationship between salt-marsh foraminifera and tidal elevation. Transects were positioned to systematically sample the elevational gradient and capture the diversity of botanical zones present at the site. The elevation of each sample was measured relative to local tidal datums by levelling (with a Leica GS15 real-time kinematic GPS utilising a base and rover; elevation error ± 0.02 m) directly to a permanent tidal benchmark (West Jamestown, RI 3742 A 1977) located ~ 1 km from Fox Hill Marsh. The elevation of the real-time kinematic GPS base station was processed using OPUS, which was then used in the Leica GeoOffice software to obtain elevations for each sample collected by the rover.

Collected sediment samples were immediately placed into a

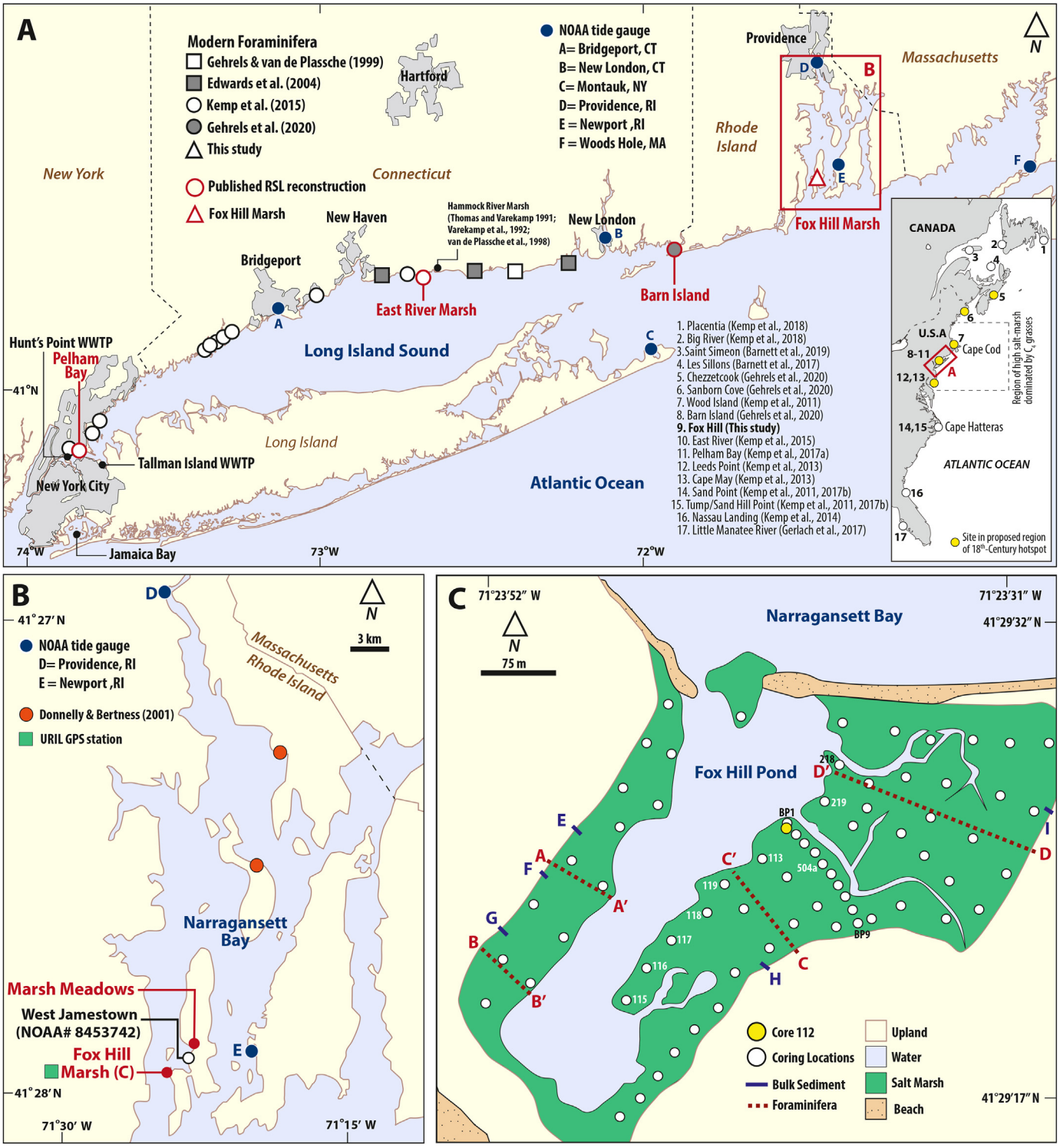

Fig. 1. **(A)** Location of study sites in southern New England. The relationship between foraminifera and tidal elevation is constrained by 315 samples collected along intertidal transects at 17 sites (greyscale symbols). Historic relative sea-level trends are measured by a network of tide gauges (blue-filled circles identified by letters). Sites with near-continuous relative sea-level reconstructions developed from cores of salt-marsh sediment are Pelham Bay, NY (Kemp et al., 2017a), East River Marsh, CT (Kemp et al., 2015), Barn Island, CT (Donnelly et al., 2004; Gehrels et al., 2020), and Fox Hill Marsh, RI (this study). WWTP = waste-water treatment plant. **(B)** Tidal datums at the Fox Hill site are assumed to be the same as those measured by the NOAA tide gauge at nearby West Jamestown. Surface samples for measuring the compression properties of salt-marsh sediment are from East River Marsh, CT and two sites in Narragansett Bay (Fox Hill Marsh and Marsh Meadows). **(C)** The stratigraphy beneath Fox Hill Marsh was described from hand-driven sediment cores and core FHM-112 was selected for detailed analysis. Four intertidal transects (labelled A–D) were used to document the modern distribution of foraminifera. Bulk sediment $\delta^{13}C$ was measured in samples collected along five short transects spanning the transition from freshwater upland to high salt marsh (E–I). References cited in body of figure are (Barnett et al., 2017, 2019; Edwards et al., 2004; Gehrels and van de Plassche, 1999; Kemp et al., 2017a,b) (For interpretation of the references to color in this figure legend, the reader is referred to the Web version of this article.)

buffered ethanol solution containing rose Bengal to stain living individuals (Walton, 1952) and then stored at 4 °C in darkness. Samples were analysed within six months of collection. In the laboratory, each sample was sieved to isolate sediment between 63 μm and 500 μm and then divided into eight representative subsamples using a wet splitter (Scott and Hermelin, 1993). We counted foraminifera until reaching at least 100 dead individuals (unstained), or until the sample was depleted. Dead assemblages are used to capture a time-average assemblage that reduces the influence of seasonality and patchiness (e.g., Scott and Medioli, 1980; Horton, 1999). Samples containing fewer than 40 dead foraminifera were excluded from further analyses because they may be statistically unrepresentative of downcore assemblages with the potential to return an unreliable PME reconstruction (Kemp and Telford, 2015; Kemp et al., 2020). Taxonomy followed Edwards and Wright (2015) and Wright et al. (2011).

The counts of foraminifera from Fox Hill Marsh were taxonomically standardized and added to an existing regional-scale training set compiled from sites in New York and Connecticut (Kemp et al., 2015 and references therein; Fig. 1A). In addition, we standardized and added a recently-published dataset of modern salt-marsh foraminifera from Barn Island, Connecticut (Gehrels et al., 2020). Specifically, *Trochammina inflata* and *Siphotrochammina lobata* were merged into a single taxon, as were all species of the genus *Haplophragmoides*. Individuals of the genus *Ammobaculites* were placed into a single group as tests are often broken in fossilized sediments and difficult to identify to the species level. We use *Jadammina macrescens* (rather than *Entzia macrescens* (Filipescu and Kaminski, 2011); discussion of genetic variations in Appendix 1 of Schonfeld and Mendes, 2022); because it continues to be widely used in the sea-level literature and this is the taxonomy employed in the pre-existing database of modern assemblages (Kemp et al., 2015 and references therein). To enable sites with different tidal ranges to be combined, we express sample elevation using a standardized water level index (SWLI), where a value of 0 corresponds to local mean tide level (MTL) and a value of 100 is local MHHW. Therefore, the elevation of MHW varies among sites (88 SWLI at Fox Hill Marsh). We designated the highest occurrence of foraminifera (HOF) to be the single highest sample in the regional-scale modern training set. We could not use HOF in standardizing elevation since it was not captured in all of the transects in the modern training set (Wright et al., 2011).

3.1.2. Stable carbon isotopes in bulk sediment

Salt-marsh grasses have different tolerances to the duration and frequency of tidal inundation and consequently form conspicuous vegetation zones (e.g., Bertness, 1991; Johnson and York, 1915; Redfield, 1972). Along the U.S. Atlantic coast from approximately Delaware to southern Maine (Fig. 1A inset), salt-marsh floral zones below MHHW are occupied primarily by grasses using the C_4 photosynthetic pathway, while zones above MHHW are dominated by C_3 plants (e.g., Johnson et al., 2007; Kemp et al., 2010; Kemp et al., 2012b; Middleburg et al., 1997; Walker et al., 2021). The degree of fractionation in favor of $^{12}CO_2$ over $^{13}CO_2$ by C_3 plants is greater than it is by C_4 plants, resulting in characteristic and readily-distinguishable $\delta^{13}C$ differences between these two groups (e.g., Lamb et al., 2006). Deposition of *in-situ* organic material is a primary mechanism of sediment accumulation in southern New England salt marshes and bulk sediment therefore carries a $\delta^{13}C$ signature that reflects the dominant plant community at the time of deposition (e.g., Chmura and Aharon, 1995; Middleburg et al., 1997; Tanner et al., 2010). Post-depositional changes to bulk-sediment $\delta^{13}C$ values are smaller than the difference between modern depositional environments dominated by C_3 and C_4 plants (Benner et al., 1987; Gebrehiwet et al., 2008; Johnson et al., 2007).

To determine a local threshold $\delta^{13}C$ value for differentiating between communities of C_4 grasses found below MHHW and C_3 plants found above MHHW, we collected bulk surface-sediment samples along five transects at Fox Hill Marsh (Fig. 1C). Six samples on each transect captured the transition from the high salt-marsh platform to surrounding freshwater upland, including brackish, transitional communities of *I. fructescens, P. australis, Typha* spp., and/or *Schoenoplectus* spp. Sample elevations were measured using the method and instruments described in section 3.1.1. Samples were stored at 4 °C and in darkness to prevent degradation before being oven dried at ~40 °C and ground to a fine, homogenized powder. Approximately 2 cm^3 subsamples of dried sediment were treated with 5 ml of 6 N (20% weight for weight (w/w)) HCl for 12 h at room temperature to remove any carbonate. Samples were then neutralized with de-ionized water and dried. $\delta^{13}C$ and total organic carbon content (TOC) were measured using an Isoprime 100 Isotope Ratio Mass Spectrometer interfaced with a Micro Vario Elemental Analyzer. The carbon isotope composition is expressed as a part per thousand deviation from the Vienna Pee Dee Belemnite standard ($\delta^{13}C$ ‰, VPDB). Modern photosynthesizing plants draw CO_2 from an atmosphere that was enriched in ^{12}C through combustion of fossil fuels (the Suess effect; Keeling, 1979). Consequently, the isotopic composition of the atmosphere changed from −6.4‰ in 1845 CE (Francey et al., 1999) to −8.6‰ in 2017 CE (at Mauna Loa; Keeling et al., 2001). To improve the analogy between $\delta^{13}C$ values measured in modern and fossil samples (Wilson, 2017), we adjusted modern measurements for the Suess effect by adding 1.86‰, which is the decadal average correction for 2010–2020 CE during which the samples were collected. We refer to these adjusted measurements as $\delta^{13}C_{adj}$. The 1.86‰ value was calculated from annual atmospheric measurements collated in Linsley et al. (2019).

3.2. Sediment coring

The stratigraphy beneath Fox Hill Marsh was mapped from ~60, hand-driven sediment cores positioned along transects (Fig. 1C) and described in the field using Troels-Smith (1955). We selected core FHM-112 for further analysis because it contained a thick unit of high salt-marsh peat (with abundant, *in-situ* macrofossils for radiocarbon dating) that we considered likely to provide a detailed RSL spanning the past ~3000 years. We collected the core in overlapping, 50-cm long increments with an Eijkelkamp peat sampler (52 mm diameter) to reduce contamination and sediment compaction during core recovery. All core samples were transferred to split PVC tubes, wrapped in plastic, labelled, and stored at 4 °C for preservation. Core-top elevations were measured using the method and instruments described in section 3.1.1.

3.3. Core chronology

We isolated identifiable and *in-situ* rhizomes and stems of salt-marsh plants (primarily *D. spicata*) for radiocarbon dating by dissecting FHM-112 at every 1-cm thick interval (Donnelly, 2006; Kemp et al., 2013b; van de Plassche et al., 1998). These macrofossils grew up to 4 cm below the salt-marsh surface and are therefore appropriate material for radiocarbon dating paleomarsh surfaces (van de Plassche et al., 1998; Wright et al., 2017) that were inhabited by the salt-marsh foraminifera that we used to reconstruct PME (section 3.4). From the suite of available macrofossils, we selected samples to provide an approximately even spacing of radiocarbon dates throughout the core. These samples were cleaned under a microscope to remove any younger root material and adhered sediment and then oven dried at ~40 °C. At the National Ocean Sciences Accelerator Mass Spectrometry facility,

samples underwent acid-base-acid pretreatment before conversion to graphite; $\delta^{13}C$ was measured on an aliquot of gas collected during sample combustion.

Due to a plateau in the radiocarbon calibration curve, material younger than ~1600 CE returns multiple calibrated ages resulting in relatively large chronological uncertainty (Reimer et al., 2020). To overcome this impediment to developing a precise chronology of sediment accumulation in FHM-112, we identified pollution trends and events of known age in downcore profiles of lead isotope ratios, metals concentrations, and ^{137}Cs activity from the upper 70 cm of FHM-112. Lead isotope ratios and metals concentrations were measured by mass spectrometry at a commercial laboratory (SGS Mineral Services). We sampled and processed the core at 1 cm increments (0–20 cm depth) and measured ^{137}Cs activity in sample thicknesses combined as necessary to achieve sufficient mass to fill the standard counting geometry (i.e., sealed Petri dish) using the methods and instruments described in Corbett and Walsh (2015).

Downcore trends of lead isotope ratios, metals concentrations, and ^{137}Cs activity were assigned to known historical pollution trends/events with several assumptions. Atmospheric deposition (via prevailing westerlies) is the principal source of metal input to high-marsh sediments (Bricker-Urso et al., 1989). We assume that no further isotopic fractionation took place during transport, or following deposition on the marsh surface (Kemp et al., 2012a; Lima et al., 2005). Downcore trends are interpreted primarily as regional-, rather than local-scale trends (Dunnington et al., 2020). Trends rather than absolute values are used because pollution per unit of production and sedimentation rate can vary through time. Age uncertainties assigned to each age marker account for the time between pollution emission and subsequent deposition. Depth uncertainties reflect the interval in the core over which a trend or event occurred.

We produced an age-depth model for FHM-112 using Bchron (Parnell et al., 2008, 2011; Parnell and Gehrels, 2015). The position of radiocarbon-dated macrofossils was adjusted upward by 2 cm and assigned an uncertainty of ±2 cm since they grow within 4 cm of the salt-marsh surface. The Bchron age-depth model calibrated these ages using the IntCal20 calibration curve (Reimer et al., 2020). Horizons dated by recognition of pollution trends and events were treated as having normally distributed uncertainty.

3.4. Reconstructing relative sea level

We counted foraminifera preserved in 1-cm thick samples positioned at 3-cm intervals, with additional samples counted in a section of the core (47–31 cm) corresponding approximately to the 18th century. Methods followed those described for modern samples (section 3.1.1), except that no rose Bengal stain was added. The analogy between modern and fossil assemblages of foraminifera was quantified using 12 dissimilarity measures. This analysis was performed using the *analogue* package for R (Simpson, 2007, 2012). For each method, the dissimilarity between all possible pairs of modern samples was measured and the 20th percentile of these values was adopted as a threshold (Kemp and Telford, 2015). If the dissimilarity between a core sample and its closest modern analog exceeded the threshold it was deemed to have no modern analog, while dissimilarity less than the threshold indicated acceptable analogy between modern and fossil assemblages. Samples without a modern analog under at least six of the 12 dissimilarity metrics were removed from further analysis.

At 5-cm intervals we measured bulk sediment $\delta^{13}C$ using the instruments and methods described for surface sediment (section 3.1.2). The Bchron age-depth model (1000 runs in the final ensemble, which is the default setting) estimated the age of each $\delta^{13}C$ sample in the core and we used this age to correct for the Suess effect using decadal-average values since 1840 CE (Linsley et al., 2019). Consequently, all modern and core $\delta^{13}C$ values are corrected to pre-anthropogenic values and are directly comparable regardless of age.

PME was reconstructed using a Bayesian transfer function (BTF; Cahill et al., 2016) trained on the expanded dataset of modern foraminifera (section 3.1.1; Fig. 2). We used *n*-fold cross validation to assess BTF performance, during which 10% of modern samples (i.e., n = 10) were removed from the training set and predicted. Downcore $\delta^{13}C$ values provided informative priors to constrain model estimates of PME (Cahill et al., 2016; Kemp et al., 2017a). Rather than use individual $\delta^{13}C$ measurements to set priors, we divided the core into sections characterized by persistent values and assigned each depth with counts of foraminifera one of three possible priors. (1) Samples where $\delta^{13}C$ values (more positive than −17.0‰) and lithology (peat) indicate deposition on the high salt-marsh platform dominated by C_4 grasses were assumed most likely to have accumulated between MHW and MHHW (88–100 SWLI). (2) If $\delta^{13}C$ values (more negative than −20.0‰) indicate an environment of deposition dominated by C_3 plants, the specified prior elevation was MHHW to HOF (100–165 SWLI). (3) Intermediate $\delta^{13}C$ values (−17.0‰ to −20.0‰) provide no additional information and no informative prior was assigned. These threshold values were established empirically (see section 4.2). Application of the BTF to downcore assemblages of foraminifera estimated PME with uncertainty (95% credible interval), which was converted from SWLI units using the modern tidal range at the study site. This approach therefore assumes a stationary inundation regime.

RSL is calculated using the following equation:

$$RSL = Altitude_i - PME_i$$

Where $Altitude_i$ is the measured contemporary elevation of the sample *i* (core top minus depth in core) and PME_i is the paleomarsh elevation reconstructed by the BTF (both terms expressed relative to the same tidal datum). Therefore, 0 m RSL is, by definition, achieved in the year of core collection since Altitude and PME for the surface sample in FHM-112 should have the same value (within uncertainty). The age (with uncertainty expressed as a 95% credible interval) of sample *i* is estimated by the age-depth model.

3.5. Quantifying relative sea-level trends

Tide-gauge measurements from Newport, Providence, New London, Woods Hole, and Montauk (Fig. 1A) provide an instrumental record of historical RSL change. Annual measurements were first averaged spatially across these five locations and then averaged temporally to produce a decadal-resolution dataset (with an associated vertical and chronological uncertainty) that could be meaningfully combined with the proxy reconstruction. We initially used an Errors-in-Variables Integrated Gaussian Process (EIV-IGP) model to quantify RSL trends with uncertainties (Cahill et al., 2015). Input for the EIV-IGP model was the proxy RSL reconstruction from FHM-112 and the decadal-average RSL data compiled from regional tide-gauge measurements. We also applied the statistical model presented in Gehrels et al. (2020) to explore how model architecture and choice can influence interpretation of proxy RSL histories. For convenience we refer to this as the G20 model. The EIV-IGP and G20 models are described more fully (and directly compared) in section 5.2. We employed the approach and model used by Walker et al. (2022) to identify when modern rates of sea-level rise began (termed time of emergence) and to quantify global, regional, and local sea-level budgets. The input data of RSL reconstructions for this analysis was the database of proxy sea-level reconstructions used by Walker et al. (2022) following updates to include the new

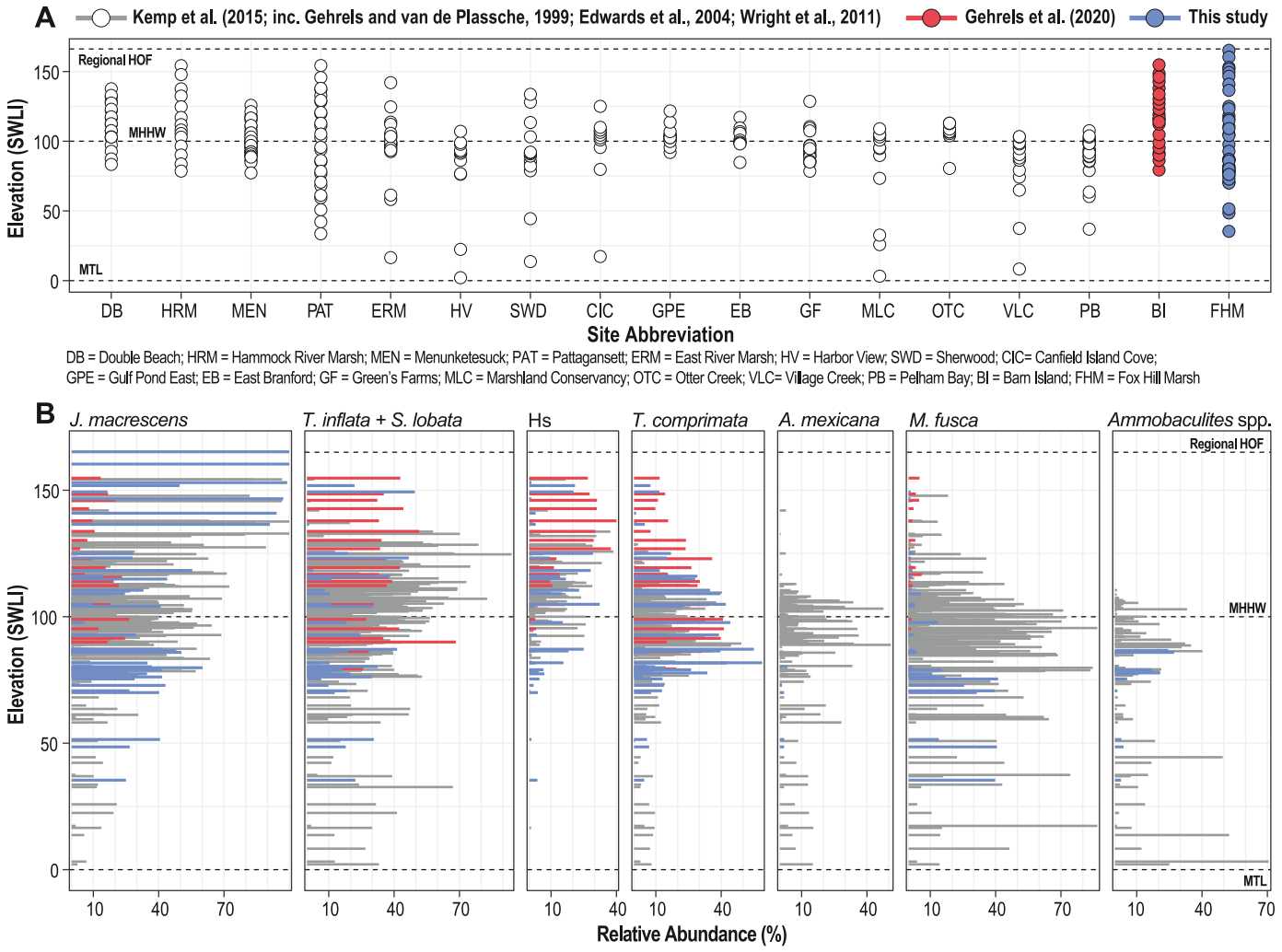

Fig. 2. Regional-scale modern training set of salt-marsh foraminifera used in the Bayesian transfer function. **(A)** The training set is comprised of 315 samples collected along transects at 17 sites in New York, Connecticut, and Rhode Island. The data collected and compiled from previous studies by Kemp et al. (2015) was updated to include more recent data from Barn Island (BI; Gehrels et al., 2020) and Fox Hill Marsh (FHM; this study). Sample elevation is expressed as a standardized water level index (SWLI), where a value of 0 corresponds to local mean tide level (MTL) and a value of 100 is local mean higher high water (MHHW). The single highest sample containing foraminifera is used to define the regional highest occurrence of foraminifera (HOF) as 165 SWLI. **(B)** Relationship between major taxa and tidal elevation in the regional-scale modern training set. Hs = *Haplophragmoides* spp. For clarity of presentation, only the recent additions to the modern training set from Barn Island and Fox Hill Marsh are differentiated by color from the previous compilation. (For interpretation of the references to color in this figure legend, the reader is referred to the Web version of this article.)

record from Fox Hill Marsh and modified versions of the East River and Pelham Bay reconstructions (see section 3.7).

3.6. Post-depositional lowering

Salt-marsh sediments can experience post-depositional lowering (PDL) through physical compaction and mass loss during biodegradation (Bloom, 1964; Brain, 2016; Long et al., 2006) with the effect that the magnitude and rate of reconstructed RSL rise is over estimated (e.g., Shennan and Horton, 2002). We estimated PDL caused by physical compaction of samples in FHM-112 using the geotechnical modelling approach of Brain et al. (2015, 2011, 2012). This approach requires a modern training set of surface sediment samples to inform and run the geotechnical model, for which we used an existing dataset of 11 salt-marsh samples from East River Marsh (Brain et al., 2017, Fig. 1) supplemented with four new samples from two sites in Rhode Island (Fox Hill Marsh and Marsh Meadows; Fig. 1B). We measured organic content (loss-on-ignition; LOI), particle density (G_s), and compression behavior using the methods and instruments described in Brain et al. (2017; Table 1). The expanded modern dataset of 15 surface sediment samples comprised the empirical observations needed to quantify the relationship between LOI and compression properties of salt-marsh sediment using regression models (Table 2).

For contiguous, 2-cm thick samples in FHM-112, we measured LOI and dry bulk density and then used the empirical relationships established from modern, analogous sediments to estimate the compression properties at each sample depth (Table 2). For each modelled layer in each model run, we assigned values of the compressive yield stress (σ'_y) by sampling from a continuous triangular probability distribution, defined by the modal value and range of σ'_y observed in surface sediments tested. The geotechnical model was implemented using a Monte Carlo approach (5000 runs) to estimate PDL with uncertainty (±1 standard deviation) for the core samples. We compared measured and model-derived estimates of dry bulk density to assess model performance.

Table 1
Key geotechnical and material properties of modern samples collected at Fox Hill Marsh and Marsh Meadows, Rhode Island.

Sample ID	Loss on ignition (%)	Particle density, G_s	Voids ratio at 1 kPa, e_1	Recompression index, C_r	Compression index, C_c	Yield stress, σ'_y (kPa)
FHM13-GT01	50.15	2.15	8.39	0.02	3.51	2.50
FHM13-GT02	42.83	2.08	12.87	0.05	5.22	2.50
JMT-13-GT01	52.14	1.94	8.24	0.09	3.40	3.00
JMT-13-GT02	56.56	2.22	16.64	0.18	6.48	3.00

Table 2
Summary of error terms for regression equations used in decompaction modelling. All predicted variables are unitless.

Predicted variable	Residuals passed Shapiro-Wilk normality test?	Regression model error distribution	± error term	Equation
G_s	No	Uniform	0.25[a]	$G_s = \frac{3.8}{(0.013 \times LOI) + 1.4}$
e_1	Yes	Normal	2.04[b]	$e_1 = 0.205 \times LOI + 1.02$
C_c	Yes	Normal	0.86[b]	$C_c = 0.092 \times LOI - 0.019$

[a] Error term is ± half range of residuals.
[b] Error term is ± 1 standard error.

3.7. Modifications to existing relative sea-level reconstructions

Gehrels et al. (2020) proposed that additional (e.g., Fox Hill Marsh) and more detailed RSL (i.e., revision of existing records) reconstructions from southern New England would be valuable for testing their hypothesis that a hotspot of rise occurred during the 18th century and was caused by melting of land-based ice in the Arctic. To meet this need, we updated existing RSL reconstructions (shown on Fig. 1A) from Pelham Bay, NY (Kemp et al., 2017a) and East River Marsh, CT (Kemp et al., 2015), that were excluded from the analysis by Gehrels et al. (2020) on the basis of having insufficient resolution. We generated a new age-depth model for core PBA-4 from Pelham Bay using the Bchron package. We used the chronological data of Kemp et al. (2017a), but with an additional age marker representing the historic impact of wastewater treatment plants on the amount and isotopic composition of nitrogen deposited in nearby salt-marsh sediment. Peteet et al. (2018) proposed that nitrogen concentration and $\delta^{15}N$ were negatively correlated in pre-anthropogenic sediment, but discharge of wastewater resulted in a positive correlation because bacteria preferentially process ^{14}N during denitrification resulting in discharged water being enriched in ^{15}N. They dated this change in salt-marsh sediment to 1903 CE when the Jamaica Bay wastewater treatment plant opened close to their study site (southern coast of Long Island; Fig. 1A). Since Pelham Bay is located on the northern coast of Long Island Sound it is unlikely that it received significant quantities of wastewater from the Jamaica Bay plant. The first large wastewater treatment plants closer to Pelham Bay opened at Tallman Island in 1939 and Hunts Point in 1954 (Fig. 1A). In PBA-4 a positive excursion in $\delta^{15}N$ begins at depths of 36–27 cm. Following Peteet et al. (2018), we assigned this depth interval an age of 1947 CE ± 7 years based on when nearby wastewater treatment plants opened. The new age-depth model employed the IntCal20 calibration curve (Reimer et al., 2020) for radiocarbon ages. We also updated the age-depth model for the East River RSL reconstruction by using IntCal20.

To increase the resolution of the two RSL reconstructions in the 18th century, we counted foraminifera in six additional samples from the Pelham Bay core (at 61–51 cm, approximately 1743–1835 CE) and in six additional samples from the East River Marsh trench (at 53–35 cm, approximately 1679–1850 CE). The updated temporal distribution of samples in both records is sufficient to determine if the rate of RSL rise accelerated in the 18th century at either site. Indeed, the resolution of the Pelham Bay reconstruction cannot be increased further since every 1-cm thick sample at 64–50 cm (approximately 1668–1829 CE) was counted. The new BTF (with priors from bulk sediment $\delta^{13}C_{adj}$) was applied to the assemblages of fossil foraminifera at Pelham Bay and East River to reconstruct PME. The revised RSL reconstructions are tabulated in supporting Table S1.

4. Results

4.1. Modern foraminifera

Along the four surface transects established at Fox Hill Marsh, 42 samples yielded at least 40 dead individual foraminifera and we identified 13 taxa, of which seven had a relative abundance exceeding 10% in at least one sample (Supplementary Data). Above 125 SWLI, *Jadammina macrescens* was the most common taxon (Fig. 2B), while elevations at approximately 75–125 SWLI were characterized by high abundances of *T. inflata*/*S. lobata* and *Tiphotrocha comprimata*. Below ~75 SWLI, *Miliammina fusca* was the most common taxon. These new paired observations of surface elevation and foraminifera were combined with an existing compilation of data for New York and Connecticut (Kemp et al., 2015 and references therein) and a recent dataset from Barn Island (Gehrels et al., 2020) to generate a regional-scale training set comprised 315 samples from 17 sites (Fig. 2). The new observations from Fox Hill Marsh raise the elevation of HOF from 155 SWLI to 165 SWLI in comparison to Kemp et al. (2015). At Fox Hill Marsh, the elevation of HOF therefore lies ~0.05 m above highest astronomical tide. The data from Barn Island (Gehrels et al., 2020) increase the relative abundances of *T. inflata*/*S. lobata* and *Haplophragmoides* spp. at elevations above ~125 SWLI.

We used the expanded modern training set to develop a BTF. Under *n*-fold cross validation, measured sample elevation is accurately predicted (within the 95% credible interval) for 312 of the 315 modern samples (Fig. 3A). The mean difference between observed and predicted elevation is < 5 SWLI. Above ~40 SWLI there is no discernible structure to the residuals indicating that the BTF can accurately reconstruct PME (Fig. 3B). Below ~40 SWLI, the BTF point estimates appear to over predict SWLI, but the observed elevation lies within the BTF uncertainty intervals for all but three (i.e., <1%) samples. The relationship between elevation and key taxa is quantified using species response curves (Fig. 3C). *J. macrescens* is commonly the most abundant species of foraminifera in modern and fossil sediment that was deposited in a high salt-marsh environment and quantifying its distribution with respect to tidal elevation is therefore a key step in reconstructing PME. In the

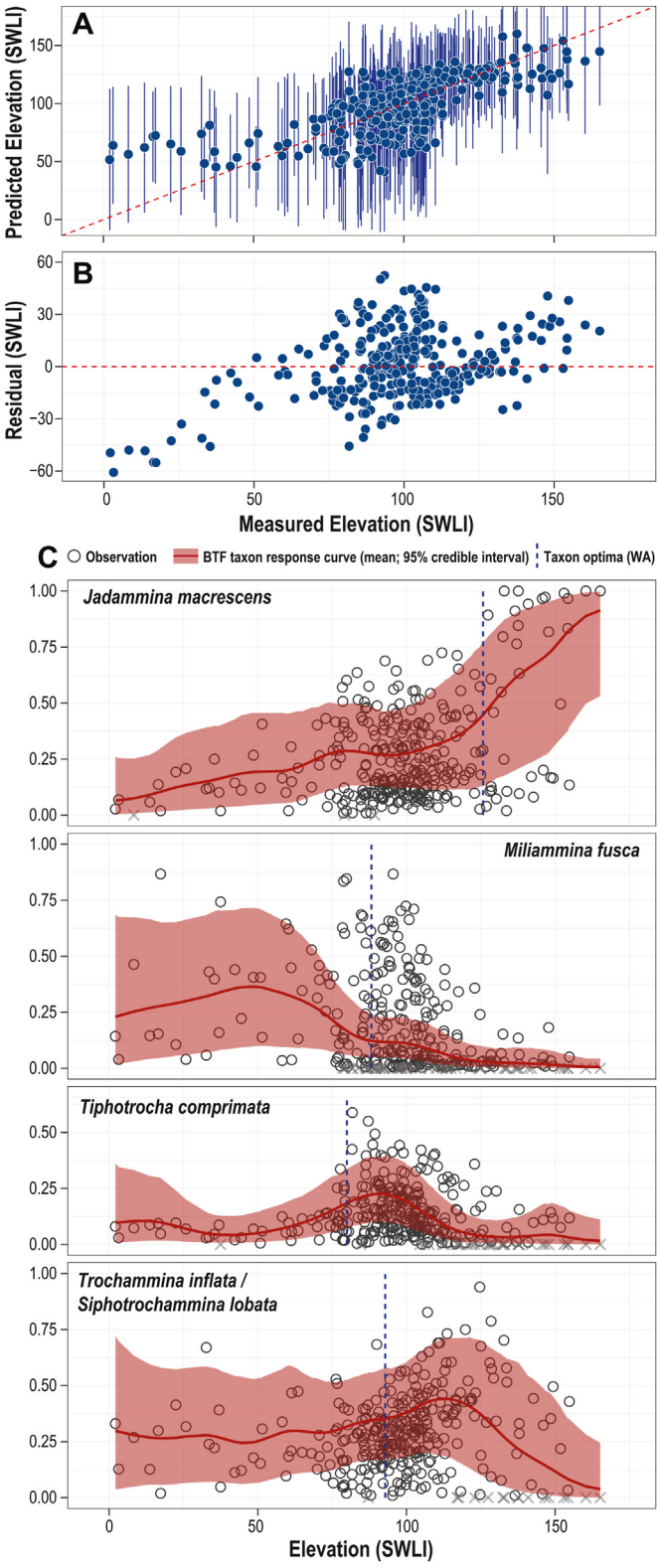

Fig. 3. **(A)** Comparison of observed (measured at the time of sample collection) and predicted (by the Bayesian transfer function under n-fold cross validation) elevation for the 315 samples from 17 salt marshes in the modern training set. Vertical error bars are the 95% credible interval for predicted elevations. Dashed line represents parity between observed and predicted elevation. SWLI = standardized water level index, where a value of zero is mean tide level and a value of 100 is mean higher high water. **(B)** Residual (observed less predicted) elevation. **(C)** Modern relationship between the four most common taxa of foraminifera in FHM-112 and tidal elevation (species response curves) quantified by the Bayesian transfer function. Circles represent observational data, solid line and shaded envelope are the model mean and 95% credible interval respectively. For comparison, the vertical dashed line represents the optima of each species calculated using a weighted averaging transfer function, which assumes a unimodal relationship between taxa abundance and elevation.

modern training set, the abundance of *J. macrescens* increases sharply at MHHW (100 SWLI) and attains a peak at HOF (165 SWLI). Since salt-marsh foraminifera are absent above HOF (i.e., the probability of occurrence immediately decreases to zero above HOF), the relationship between *J. macrescens* and tidal elevation (at least in this study region) is not most accurately described by a unimodal distribution (Kemp et al., 2018a). *M. fusca* displays a negative correlation between abundance and tidal elevation and is ubiquitous below MHW (~88 SWLI). The species response curve indicates that a unimodal distribution may also not be the most accurate means to quantify the distribution of *M. fusca*, although this is likely because a paucity of shallow sub-tidal samples in the modern training set means that it does not capture the transition to a calcareous, marine assemblage that is observed to exist in Long Island Sound (e.g., Akpati, 1975; Buzas, 1965; Thomas et al., 2000). For *T. comprimata* and *T. inflata/S. lobata* the species response curves constrained by empirical observations from the modern training set indicate that a unimodal relationship to tidal elevation is likely appropriate.

4.2. Stable carbon isotopes in modern bulk sediment

To determine the $\delta^{13}C$ threshold in bulk salt-marsh sediment that formed above/below MHHW, we measured $\delta^{13}C$ in 30 surface samples from five transects (Fig. 4; Supplementary Data). Following adjustment for the Suess effect, $\delta^{13}C_{adj}$ values ranged from −14.4‰ to −26.3‰. Ten samples yielded $\delta^{13}C_{adj}$ values less depleted than −17.0‰, of which nine were located below MHHW on the peat-forming, high salt-marsh platform vegetated principally by communities of *S. patens* and *D. spicata*, which are both C_4 grasses. There were 13 samples with $\delta^{13}C_{adj}$ values more depleted than −20‰, of which 12 were situated above MHHW in botanical zones dominated by C_3 species that are representative of brackish environments. These threshold values are similar to those observed in a dataset from three sites in southern New Jersey (Kemp et al., 2012b) and a site in northern New Jersey (Walker et al., 2021). After combining the results from Rhode Island and New Jersey (also corrected for the Suess effect), we find that 56 of 63 samples with $\delta^{13}C_{adj}$ values less depleted than −17.0‰ were collected below MHHW. Of the 41 samples with $\delta^{13}C_{adj}$ values more depleted than −20.0‰, 39 were collected at or above MHHW. For samples with intermediate values (−17.0‰ to −20.0‰) ten/nine were from below/above MHHW. Based on this dataset of modern observations in three regions with similar vegetation zones, but different climates, we propose that foraminifera-bearing sediment with a $\delta^{13}C_{adj}$ value more negative than −20.0‰ formed above MHHW but below HOF (SWLI of 100–165), while foraminifera-bearing peat with a $\delta^{13}C_{adj}$ value less negative than −17.0‰ formed between MHW and MHHW (88–100 SWLI). No constraint on tidal elevation is supported by intermediate $\delta^{13}C$ values. The spatial consistency of threshold $\delta^{13}C_{adj}$ values between Rhode Island and New Jersey indicates they are likely to be temporally robust under late Holocene climate variability.

4.3. Stratigraphy at Fox Hill Marsh

There is a consistent stratigraphy underlying Fox Hill Marsh (Figs. 1 and 5). The lowermost unit is inorganic, blue-colored silty sand and gravel that we interpret to be an incompressible substrate of glacial origin. In most locations this unit is overlain by a thin

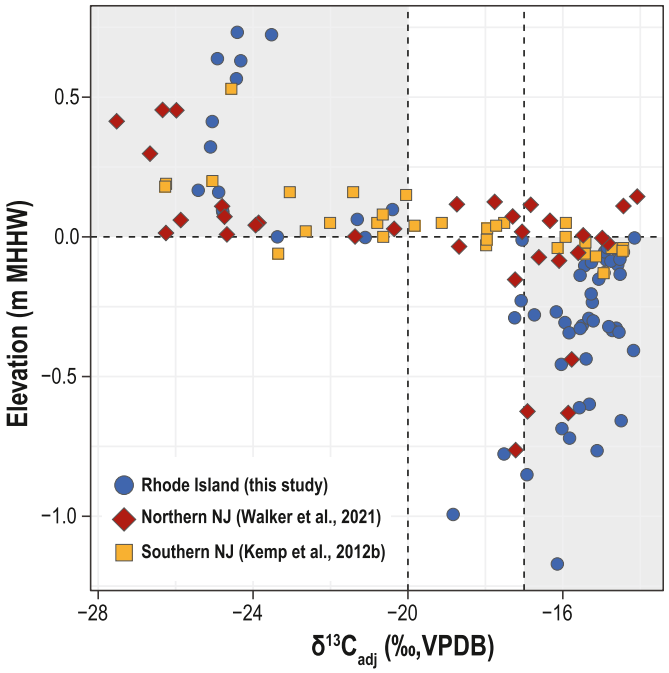

Fig. 4. Relationship between $\delta^{13}C$ values measured on bulk salt-marsh surface sediment and tidal elevation along transects at Fox Hill Marsh in Rhode Island (this study), three sites in southern New Jersey (Kemp et al., 2012b), and a site in northern New Jersey (Walker et al., 2021). Samples with $\delta^{13}C$ values (adjusted for the Suess effect; $\delta^{13}C_{adj}$) more negative than −20‰ likely accumulated above mean higher high water (MHHW), while samples less negative than −17‰ likely formed below MHHW (shaded regions). Absolute elevations are not directly comparable between Fox Hill Marsh and New Jersey because of differences in tidal range but can be reasonably used to compare $\delta^{13}C$ values above and below a single tidal datum (MHHW) that is marked by a change in botanical community in both regions.

(<20 cm) dark brown to black amorphous peat with few identifiable plant macrofossils, although in some parts of the marsh it includes relatively more sand and silt. Between this unit and the surface is a thick (up to 350 cm) interval of high salt-marsh peat with abundant, *in-situ*, and identifiable macrofossils of common salt marsh grasses, particularly *D. spicata* since its woody rhizomes are often well preserved (Niering et al., 1977). Core FHM-112 is representative of this site-wide stratigraphy and has a core-top elevation of −0.18 m MHHW (0.42 m MTL).

4.4. Chronology

We radiocarbon-dated 30 plant macrofossils (Table 3, Fig. 6). The samples were primarily identified as rhizomes of *D. spicata* and this interpretation (as well as the inference that FHM-112 accumulated on a high salt-marsh platform) is supported by $\delta^{13}C$ values measured on the macrofossils during combustion that ranged from −11.1‰ to −13.9‰, which is typical of *D. spicata* and *S. patens* tissue (e.g., Chmura et al., 1987; Choi et al., 2001; Wozniak et al., 2006). Radiocarbon dates indicate that FHM-112 spans the period since ~1200 BCE with no evidence for periods of non-deposition, erosion, or disturbance.

We identified eight chronohorizons representing pollution trends/events of known age (Table 4, Fig. 6). Stable lead isotope ratios (^{206}Pb:^{207}Pb) reflect changes in the production and use of lead in North America since the early 19th century and these trends are widely recognized in diverse sedimentary regimes in the northeastern U.S. and Canadian Maritimes (e.g., Dunnington et al., 2020; Gobeil et al., 2013; Kemp et al., 2012a), including laminated river sediment on the western coast of Narragansett Bay (<5 km from our study site; Lima et al., 2005). We assigned the age of 1858 ± 5 CE to the initial peak in $^{206}Pb/^{207}Pb$, which reflects peak lead production (as a proportion of U.S. national output) in the Upper Mississippi Valley where galena ore has a distinctive ^{206}Pb:^{207}Pb composition. A minimum and recent maximum in $^{206}Pb/^{207}Pb$ are attributed to isotopic differences in the sources of lead used in gasoline (1965 ± 5 CE) and the phasing out of leaded gasoline (1980 ± 5 CE) respectively (Bollhöfer and Rosman, 2001; Hurst, 2000; Lima et al., 2005). The initial occurrence and peak of ^{137}Cs activity are assigned ages of 1954 ± 2 CE and 1963 ± 1 CE respectively, which reflect the start of nuclear weapons testing and

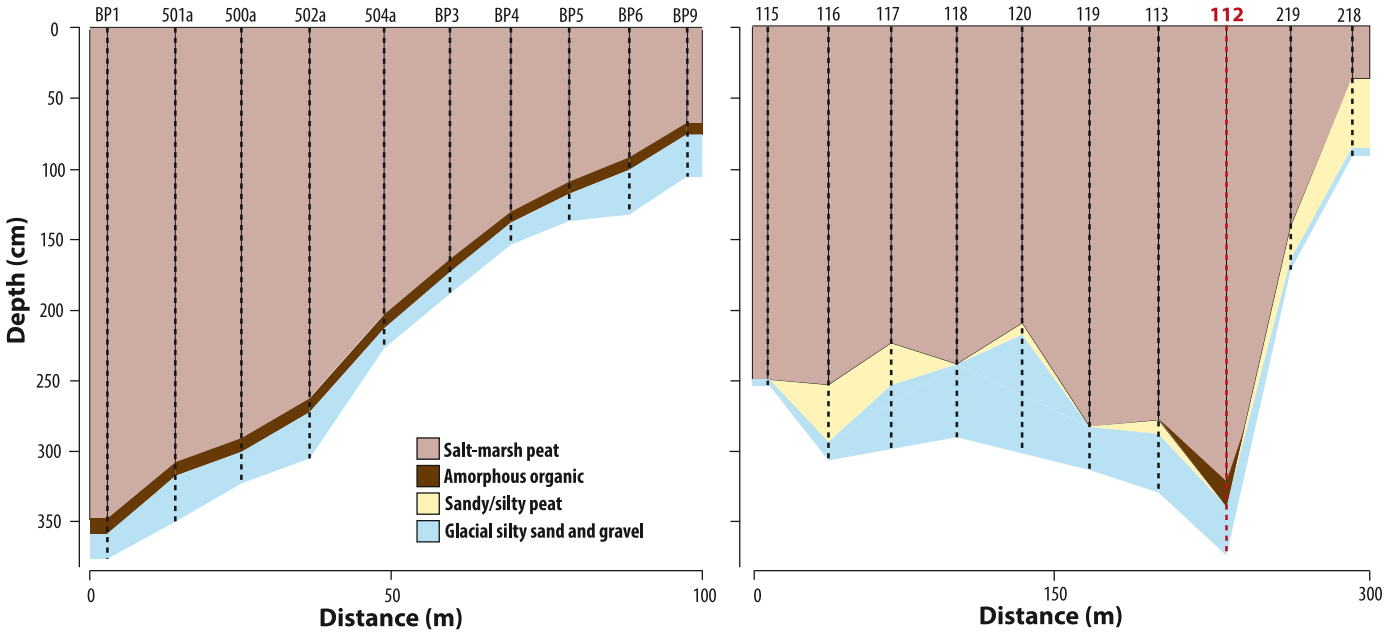

Fig. 5. Stratigraphy beneath Fox Hill Marsh along two example transects of hand-driven cores that are representative of the shallow sub surface. Core FHM-112 was selected for detailed analysis and recovered using an Eijelkamp peat sampler.

Table 3
Reported radiocarbon ages for samples in the Fox Hill Marsh core. Samples identified by the prefix "OS" were dated at the U.S. National Ocean Sciences Accelerator Mass Spectrometry laboratory and reported ages and errors were rounded following the conventions of Stuiver and Polach (1977). Sample $\delta^{13}C$ values are provided relative to the Pee Dee Belemnite (PDB) standard. Sample depths listed in table include a 2-cm adjustment for dating of plant remains that lived beneath the paleo salt-marsh surface. Samples described as plant stem were not identified to the species level. Ds = *Distichlis spicata*.

Depth (cm)	Radiocarbon Age	Radiocarbon Age Error	$\delta^{13}C$ (‰, PDB)	Laboratory Number	Dated Material
41	155	15	−12.22	OS-128561	Ds
49	315	15	−13.14	OS-129459	Ds
56	590	15	−13.12	OS-125588	Ds
75	845	20	−13.5	OS-128562	Ds
88	780	20	−11.06	OS-124242	Ds
97	940	15	−13.63	OS-125568	Ds
108	970	15	−12.13	OS-128563	Ds
119	950	15	−12.24	OS-124244	Ds
128	1120	15	−12.1	OS-125569	Ds
143	1200	15	−12.56	OS-125589	Ds
149	1280	20	−13.02	OS-129379	Ds
162	1470	20	−12.21	OS-124245	Plant stem
177	1600	20	−13.3	OS-125590	Ds
184	1790	25	−12.92	OS-125591	Ds
201	1820	20	−13.18	OS-124243	Ds
212	1910	20	−13.26	OS-125592	Ds
223	1940	20	−13.43	OS-125668	Ds
227	2040	15	−13.57	OS-129460	Ds
233	2250	15	−13.2	OS-131667	Ds
238	2250	25	−13.75	OS-124248	Ds
246	2260	20	−13.88	OS-131668	Ds
252	2360	20	−12.67	OS-125593	Ds + Plant stem
259	2470	20	−12.79	OS-128564	Ds
269	2570	20	−13.76	OS-125594	Ds
273	2520	15	−13.4	OS-128565	Ds
283	2470	20	−12.64	OS-124249	Ds
301	2770	20	−12.51	OS-125595	Ds
322	2820	20	−13.52	OS-124246	Ds
328	2900	20	−13.08	OS-129461	Ds
336	3000	20	−12.53	OS-124247	Ds

the maximum fallout (Corbett and Walsh, 2015). The initial rise in lead, vanadium, copper, and mercury concentrations above background values was interpreted as the onset of industrial activity in the second half of the 19th century and assigned an age of 1875 ± 25 CE. The peak in their concentrations is interpreted as passage of the Clean Air Act curtailing air pollution and is assigned an age of 1974 ± 5 CE. An earlier peak in mercury is assigned an age of 1900 ± 10 CE based on the ^{210}Pb chronologies developed by Varekamp et al. (2003) from salt-marsh cores on the Connecticut coast of Long Island Sound, which recorded a regional rise in mercury concentration.

The Bchron age-depth model for FHM-112 (Fig. 6) estimated the age of every 1-cm thick interval between the surface and 340 cm with an average uncertainty (95% credible interval) of ±111 years. For the samples with counts of foraminifera that were used in the final RSL reconstruction, the uncertainty ranged from ±12 years (at 2 cm) to ± 131 years (at 23 cm).

4.5. Foraminifera and bulk sediment $\delta^{13}C$ in FHM-112

Foraminifera are absent below 337 cm in the unit of glacial silty sand and gravel, but present at all sampled depths in the overlying unit of salt-marsh peat (Fig. 7; Supplementary Data). Three samples yielded <40 foraminifera and were excluded from further analysis, 12 samples yielded 41–99 foraminifera, and 113 samples provided counts >100 individuals. Samples with low counts occurred predominantly near the base of the core (332–296 cm) and at 236–227 cm. The downcore assemblage of foraminifera is comprised primarily of four taxa that have a mean abundance of 69.3% (*J. macrescens*), 13.5% (*T. inflata*/*S. lobata*), 12.1% (*T. comprimata*), and 4.5% (*M. fusca*). Cumulatively, these four taxa account for >99% of counted individuals. At 337–281 cm, the dominant taxon was *J. macrescens* (mean 86.1%). Above 279 cm, *J. macrescens* remained the most common taxon (mean 65.9%), but was accompanied by higher abundances of *T. inflata*/*S. lobata* (mean 13.5%), which was particularly prevalent at 74–37 cm (mean 29.6%). *T. comprimata* occurs throughout the core, but with noticeable increases at 89–79 cm (mean 40.4%) and 279–239 cm (mean 23.6%). The mean abundance of *M. fusca* was <1% below 185 cm, but increased to 14.3% and 15.4% for the intervals 140–107 cm and 34–0 cm respectively. Coupled with lithology and identifiable plant macrofossils, these assemblages indicate that FHM-112 accumulated on a high salt-marsh platform that largely kept pace with RSL rise. Every assemblage of foraminifera in FHM-112 had an appropriate modern analog (Fig. 8). For one sample (at 37 cm), two measures of dissimilarity indicated a lack of a modern analog, but this sample was retained in further analysis because the other ten metrics indicated a suitable analog was available in the modern training set. The samples excluded because of count size <40 (at 230, 302, and 329 cm) had modern analogs in the training set.

Following decadal-average correction for the Suess effect, bulk sediment $\delta^{13}C_{adj}$ values in FHM-112 ranged from −13.4‰ to −26.7‰ (Fig. 7). From the base of the core, $\delta^{13}C_{adj}$ values systemically shift from −26.7‰ at 350 cm to −14.0‰ at 300 cm, indicating (along with the presence of foraminifera) a transition from a botanical environment dominated by C_3 species to one dominated by C_4 salt-marsh grasses. This change is accompanied by an increase in total organic carbon from 5.8% at 350 cm to 23.8% at 340 cm. The uppermost 300 cm of FHM-112 is characterized by consistent total organic carbon (mean 23.2%, standard deviation of 4.5%) and $\delta^{13}C_{adj}$ values (less depleted than −17.0‰) that represent *in-situ* deposition of C_4 plant material. The exception is an interval lasting ~500 years between 125 cm ($\delta^{13}C_{adj}$ = −17.7‰) and 70 cm

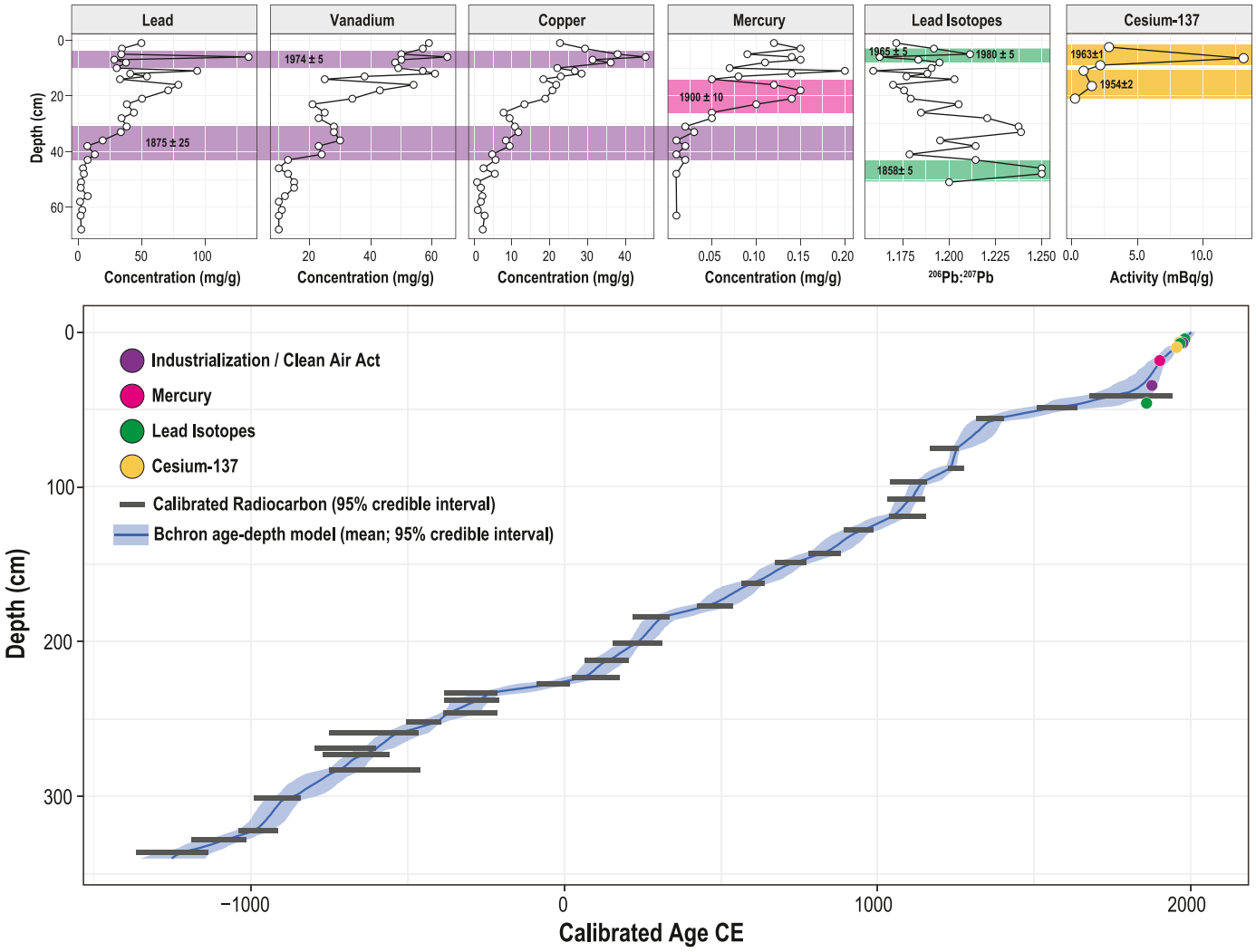

Fig. 6. Chronology for core FHM-112. Top row of panels present downcore profiles of elemental abundance, isotopic ratios, and ^{137}Cs activity used to identify historic trends and events of known age. Measurement uncertainties are smaller than symbols. Shaded envelopes represent the uncertainty in locating each historic horizon and stated ages include the uncertainty of when the trend or event occurred. The lower panel presents the Bchron age-depth model developed for FHM-112. Radiocarbon dated material was *in-situ* and identifiable plant macrofossils with a known relationship to the paleo salt-marsh surface.

Table 4
Chronohorizons identified in core FHM-112 with associated ages and depths in core.

Chronohorizon Marker	Chronohorizon Event	Age (CE)	Depth (cm)
Lead isotopes	Phasing out of leaded gasoline	1980 ± 5	4 ± 1
Cesium	Maximum fallout from nuclear weapons testing	1963 ± 1	6.5 ± 1.5
Lead, Mercury, Copper, Vanadium	Clean Air Act	1974 ± 5	7 ± 3
Lead isotopes	Variations in lead sources in gasoline	1965 ± 5	7.5 ± 2.5
Cesium	Start of nuclear weapons testing	1954 ± 2	10 ± 2
Mercury	Peak pollution in Long Island sound salt marshes	1900 ± 10	18.5 ± 3.5
Lead, Mercury, Copper, Vanadium	Industrial activity in New England	1875 ± 20	34.5 ± 7.5
Lead isotopes	Upper Missisippi Valley lead mining peak	1858 ± 5	46 ± 4

($\delta^{13}C_{adj} = -18.9‰$), when $\delta^{13}C_{adj}$ returned to the range typical of modern botanical environments dominated by C_3 plants (peak $\delta^{13}C_{adj}$ of −23.9‰ at 85 cm). This interval is not associated with a systematic change in total organic carbon and although it occurs concurrently with an increase in the abundance of *T. comprimata*, other sections of the core with elevated abundances of *T. comprimata* (e.g., 280–240 cm; Fig. 7) are not accompanied by a systematic change in $\delta^{13}C_{adj}$ values.

4.6. Reconstructing paleo marsh elevation using a Bayesian transfer function

We reconstructed PME by applying the BTF to the 125 samples in FHM-112 with count sizes >40 individuals and modern analogs in the regional-scale training set (Fig. 7). The BTF was used with uninformative priors for PME and then with priors for PME from bulk sediment $\delta^{13}C_{adj}$ values. With uninformative priors, five samples yielded a mean PME reconstruction <100 SWLI, including

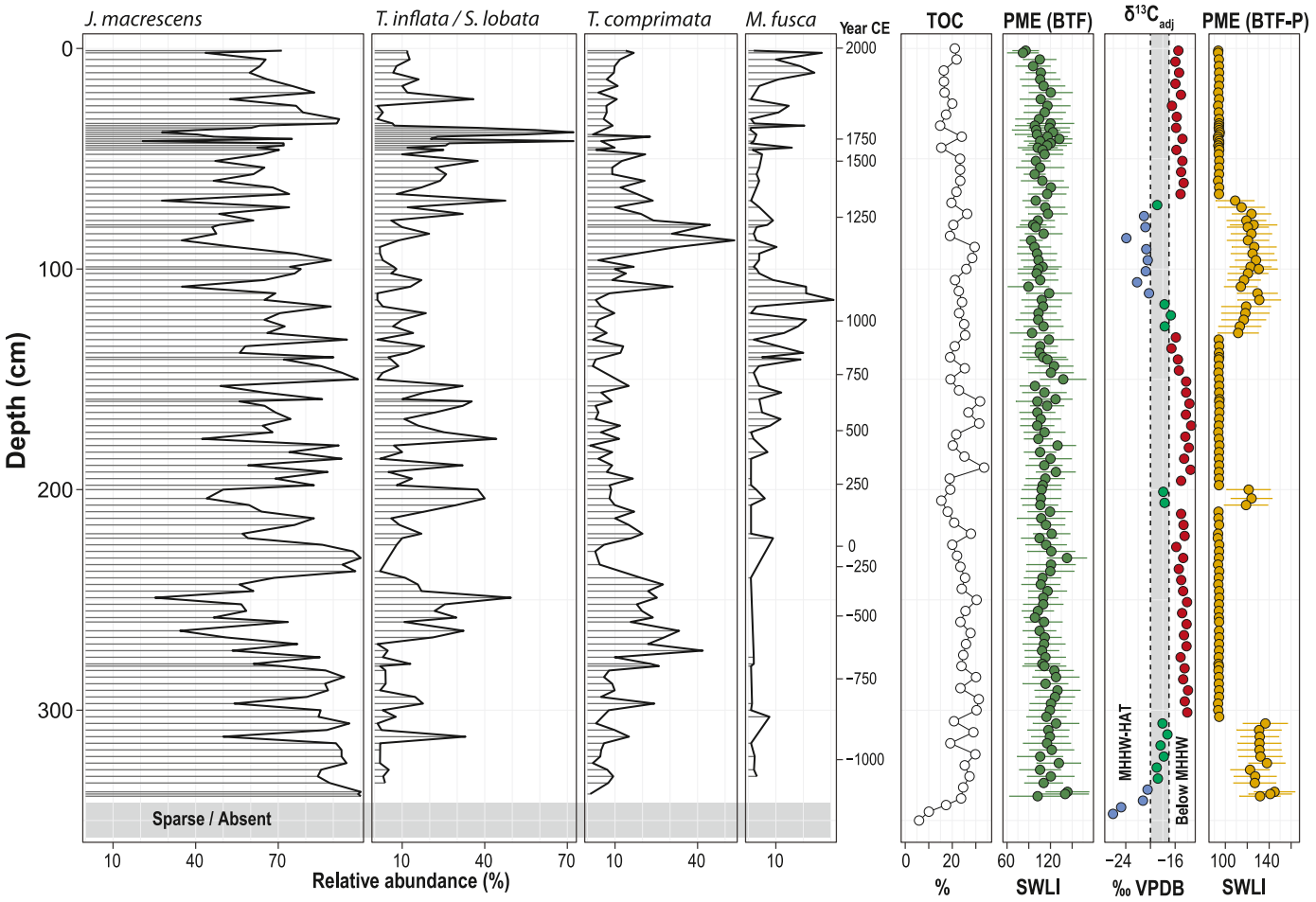

Fig. 7. Foraminifera preserved in 1-cm thick samples of core FHM-112. Total organic carbon (TOC) and $\delta^{13}C$ were measured on bulk sediment and are used to infer environment of deposition. The organic nature of all foraminifera-bearing samples indicates deposition above mean high water. Intervals of the core with $\delta^{13}C$ consistently more negative than −20‰ (vertical dashed line) likely accumulated above mean higher high water (MHHW, equating to a standardized water level index − SWLI − of 100), but below the highest occurrence of foraminifera (HOF) in the regional-scale modern training set (165 SWLI). In contrast, intervals with $\delta^{13}C$ consistently less negative than −17‰ (vertical dashed line) likely accumulated below MHHW. $\delta^{13}C$ values in the range of −17‰ to −20‰ provide no robust constraint on paleomarsh elevation (PME). Symbols in the panel presenting $\delta^{13}C$ values are colored by the prior used to constrain the Bayesian transfer function, which was used to reconstruct PME with a 95% credible interval. Results are presented for application of the Bayesian transfer function with (BTF-P) and without priors (BTF) from bulk-sediment $\delta^{13}C$ values.

three of the four samples closest to the top of the core where decreasing PME indicates recent submergence of the site by accelerating RSL rise. Excluding the samples above 10 cm, mean PME across all depths was 123 SWLI and the mean uncertainty was ±42.6 SWLI (95% credible interval). Use of informative priors from $\delta^{13}C_{adj}$ values resulted in a distinctive pattern of PME reconstructions. At depths with $\delta^{13}C_{adj}$ values more negative than −17.0‰ (below 302 cm and 143–68 cm), the BTF reconstructed PME as 132.7 ± 22.7 SWLI (mean ± one standard deviation across all depths). In contrast, specifying that samples with $\delta^{13}C_{adj}$ values less negative than −17.0‰ likely formed on a high salt-marsh platform between MHW and MHHW resulted in mean PME of 94.6 ± 10 SWLI (depths of 302–146 cm and above 68 cm).

4.7. Post-depositional lowering

Four surface sediment samples from Rhode Island yielded LOI values of 43–57% (Fig. 9A, Table 1). Existing data from East River (11 samples; Brain et al., 2017) characterized salt marsh sediment with lower organic content (9–41%; mean of 23%). We combined these two datasets to provide a regional training set to inform our geotechnical model for estimating PDL. Organic content (LOI) is positively correlated with the voids ratio at 1 kPa (e_1) ($r^2_{adj} = 0.71$; $p < 0.0001$) and the compression index (C_c) ($r^2_{adj} = 0.74$; $p < 0.0001$) in modern sediment from a range of salt-marsh subenvironments in the southern New England training set. In contrast, particle density (G_s) is negatively correlated with LOI ($r^2_{adj} = 0.69$; $p = 0.0001$) (Fig. 9; Table 2). The form and strength of the relationships between LOI and geotechnical properties is similar to those established using only the surface sediment samples from East River, but is extended to more organic sediment through inclusion of the new samples from Rhode Island salt marshes. However, there was no statistically-significant relationship between the recompression index, Cr, and LOI. As such, in our combined regional training set, values of C_r assigned to each layer were estimated from a uniform probability distribution defined by the minimum and maximum values observed in contemporary samples (Table 2 and Brain et al., 2017).

In FHM-112, inorganic samples below 348 cm were characterized by low organic content (LOI <5%) and dry density greater than 1 g/cm^3 (mean of 1.55 g/cm^3; Fig. 9F). In comparison, the overlying unit of high salt-marsh peat was more organic (mean LOI of 56% with a standard deviation of 12%) and less dense (mean dry density of 0.97 g/cm^3 with a standard deviation of 0.07 g/cm^3). Comparison

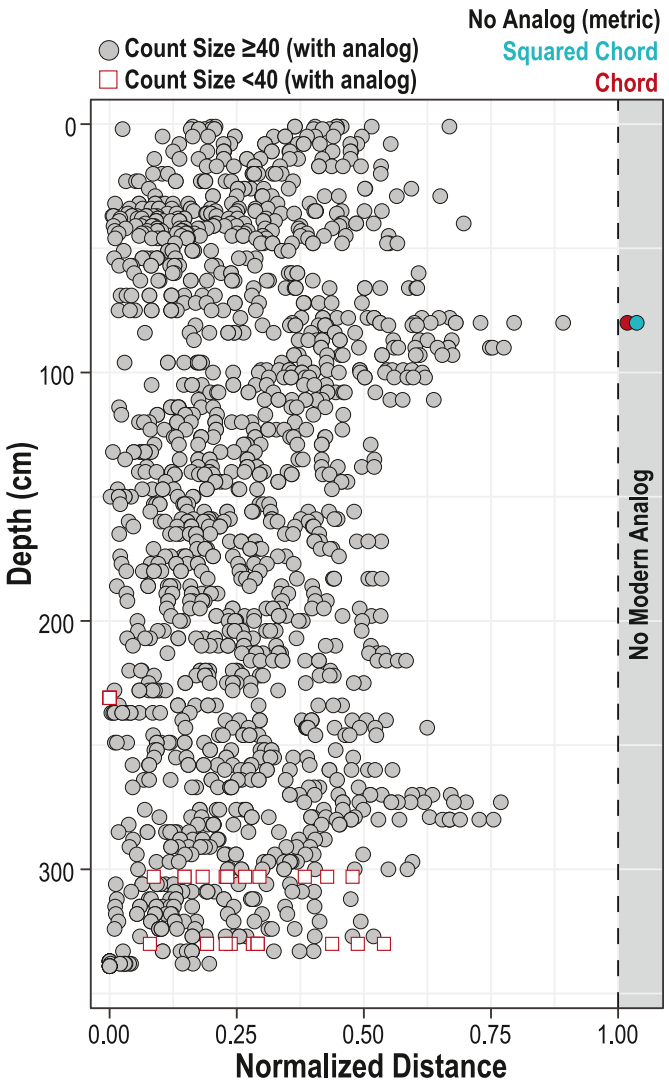

Fig. 8. Analogy between assemblages of foraminifera in 1-cm thick samples of core FHM-112 and their closest analog in the regional-scale modern training set comprised of 315 samples from 17 sites in New York, Connecticut, and Rhode Island. For each depth, a calculated value is presented for the 12 different metrics employed to measure dissimilarity. The threshold for determining if a sample has a modern analog is calculated using the 20th percentile of dissimilarity measured between all possible pairs of modern samples. Since the absolute values of these thresholds varies depending on the metric used, dissimilarity is standardized where a value of 1 is equal to the threshold. Values less than 1 indicate that a core sample has a modern analog, while values greater than 1 indicate that the sample does not have an appropriate modern analog. For clarity of presentation only symbols greater than 1 are colored by the dissimilarity metric used. Samples with fewer than 40 individuals were removed for further analysis because of low count size.

of measured and predicted dry bulk density provides a means to examine model performance. Linear regression of modelled and observed dry density yielded a strong ($r^2_{adj} = 0.92$) positive and statistically significant ($p < 0.0001$) relationship (Fig. 9E), indicative of strong model performance. Measured values of dry bulk density from the unit of salt-marsh peat lie within the 1σ uncertainty bounds of the model predictions (Fig. 9F). Although measured and predicted dry bulk density below 350 cm are comparable within uncertainty, the model systematically overpredicts dry bulk density in this clastic unit. However, this does not lead to a corresponding bias in predictions of PDL because the unit of salt-marsh peat is not overlain by, or intercalated with, horizons of dense clastic sediment. The effective stress within the sediment column increases linearly from 0 kPa at the surface to 2.3 kPa at 350 cm, below which the greater density of sediment causes a change in slope; effective stress increases more rapidly with depth to reach 3.6 kPa at 366 cm. Maximum PDL (1.1 cm ± 0.09 cm; 1σ) occurs at 216 cm. Overall, these results indicate that the salt-marsh peats in this location experienced minimal PDL (maximum average rate of ~0.5 cm per thousand years) through compaction over centennial to millennial timescales (Fig. 9F). Given the low magnitude of PDL, we do not adjust our RSL reconstruction for its influence, but we do discount physical compaction as a meaningful driver of late Holocene RSL change at Fox Hill Marsh.

4.8. Relative sea-level trends

Measurements from five tide gauges in the study region (Fig. 1) display coherent variability on annual to multi-decadal time scales and recorded average RSL rise of 2.84 mm/yr over the period 1931–2020 CE (Fig. 10A inset). The proxy reconstruction shows ~3.7 m of RSL rise at Fox Hill Marsh since ~1200 BCE (Fig. 10A). The instrumental record of historic RSL rise falls within the uncertainty of the proxy reconstruction. The principal driver of late Holocene RSL trends along the U.S. Atlantic coast is ongoing GIA, which can reasonably be approximated as linear over this time interval (Peltier, 1996). To isolate the role of other physical processes and to improve comparability among reconstructions, the estimated contribution from GIA was removed. Several lines of evidence provide a coherent estimate of the rate of GIA in southern Rhode Island. Permanent GPS stations (including station URIL located ~11 km from Fox Hill Marsh; Fig. 1A) estimate a contribution of 0.9 ± 0.2 mm/yr (Karegar et al., 2016). A database of basal (compaction-free) sea-level index points suggest that GIA is 1.1 ± 0.1 mm/yr (Engelhart and Horton, 2012; Engelhart et al., 2009). Earth-ice model predictions suggest slightly higher rates of GIA such as 1.3 mm/yr at Newport (ICE-6G_C VM5a; Peltier et al., 2015). Piecuch et al. (2018b) assimilated these lines of evidence and estimated that GIA contributed 1.06 ± 0.55 mm/yr to historic RSL rise at Newport. We removed 1.06 mm/yr from our RSL reconstruction and the compilation of tide-gauge measurements (Fig. 10B).

We quantified (multi-)century scale trends in GIA-corrected sea-level change at Fox Hill Marsh using the EIV-IGP model (Cahill et al., 2015). Mean rates of change since 1230 BCE oscillated within 0 ± 1 mm/yr until the mid-20th century (Fig. 10C). Departures from stability (95% credible interval that does not include 0 mm/yr) occurred at 1031–731 BCE (rising), 381–31 BCE (falling), 1044–1219 CE (rising), 1519–1669 CE (falling), and since 1869 CE (rising). Minor oscillations may exist between 0 and 1000 CE, but these are not distinguishable within the 95% credible intervals. The maximum rate of rise recorded was 1.71 ± 0.84 mm/yr (95% credible interval) in 2020 CE; a century-scale rate of rise unsurpassed in at least the previous 3000 years.

5. Discussion

5.1. Common Era sea-level variability

Acceleration in the rate of sea-level rise during the late 19th or early 20th centuries is a robust feature of Common Era sea-level reconstructions (e.g., Engelhart et al., 2009) and tide-gauge records (e.g.,Hay et al., 2015; Church and White, 2011). In Rhode Island this acceleration resulted in the fastest (century-scale, under the EIV-IGP model) rate of rise during at least the past 3000 years occurring in the early 21st century (Fig. 10). Following correction for GIA, the magnitude of this accelerated rate (1.71 ± 0.84 mm/yr in 2020 CE) is consistent with analysis of tide-gauge records, which

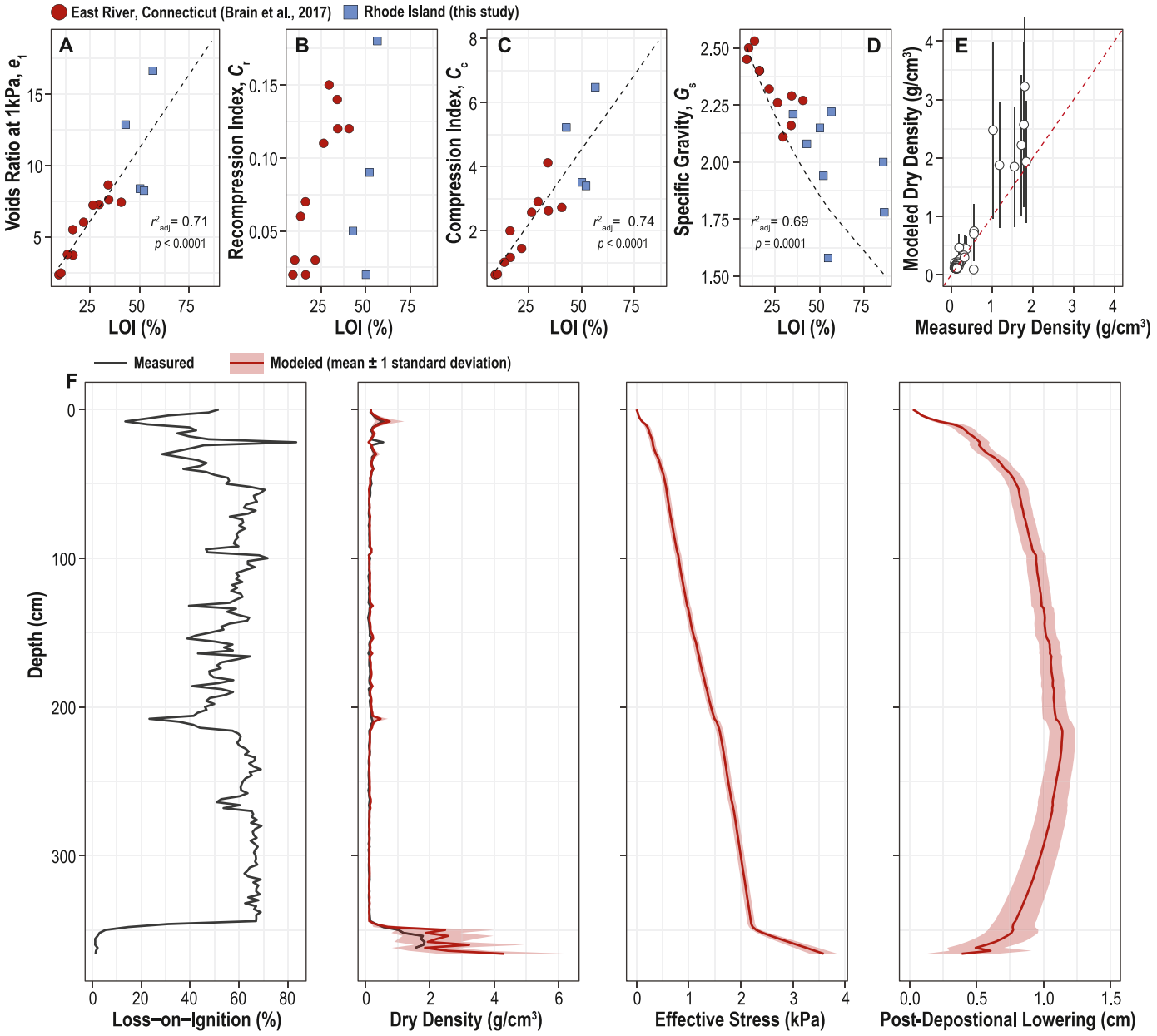

Fig. 9. Estimating post-depositional lowering in FHM-112 using a geotechnical model. **(A–D)** Relationship between organic content (measured by loss-on-ignition; LOI) and geotechnical properties of modern salt-marsh sediment at East River, CT (Brain et al., 2017) and in Rhode Island (this study; differentiated by symbol shape and fill). In D, the model equation is from Hobbs (1986). **(E)** Comparison of measured and predicted (by the geotechnical model) dry bulk density. Vertical error bars are the 1σ range of model predictions. Dashed line represents parity between observed and predicted values. **(F)** Downcore geotechnical properties and estimated post-depositional lowering (PDL).

estimated the rate of global mean sea-level rise since 1900 CE to be 1.56 ± 0.33 mm/yr (90% confidence interval; Frederikse et al., 2020). Timing of emergence analysis (Walker et al., 2022) indicates that the rate of sea-level rise at Fox Hill Marsh exceeded Common Era variability from 1918 CE onwards (1853–1945 CE; 95% credible interval). This timing is consistent with results from other sites in the study region (1750–1903 CE at Pelham Bay; 1820–1908 CE at East River Marsh; 1858–1927 CE at Barn Island). Accelerated sea-level rise is readily identifiable because it represents a large (and growing) signal relative to the contribution from GIA (Walker et al., 2022). For example, at Fox Hill Marsh GIA (1.06 mm/yr; Piecuch et al., 2018b) comprised ~90% of the total rate of century-scale RSL change in 1820 CE, compared to ~55% in 1920 CE, and ~38% in 2020 CE. Decomposition of RSL reconstructions indicates that the majority (~75%) of sea-level rise since 1900 CE in excess of GIA is from processes driving global mean sea-level change (Walker et al., 2022), such as thermal expansion and melting of land ice (particularly glaciers; Frederikse et al., 2020) resulting in a signal that is detected at large spatial scales. We conclude that the timing and magnitude of historic, accelerated sea-level rise is a robust and well-replicated feature of southern New England's sea-level history because the signal is large and widespread rendering it readily identifiable. Generating additional proxy RSL reconstructions in the northeastern United States and Canadian Maritimes is therefore unlikely to meaningfully revise our understanding of when and why accelerated sea-level rise began.

Prior to the onset of historic sea-level rise, some proxy reconstructions identified smaller-magnitude phases of century-

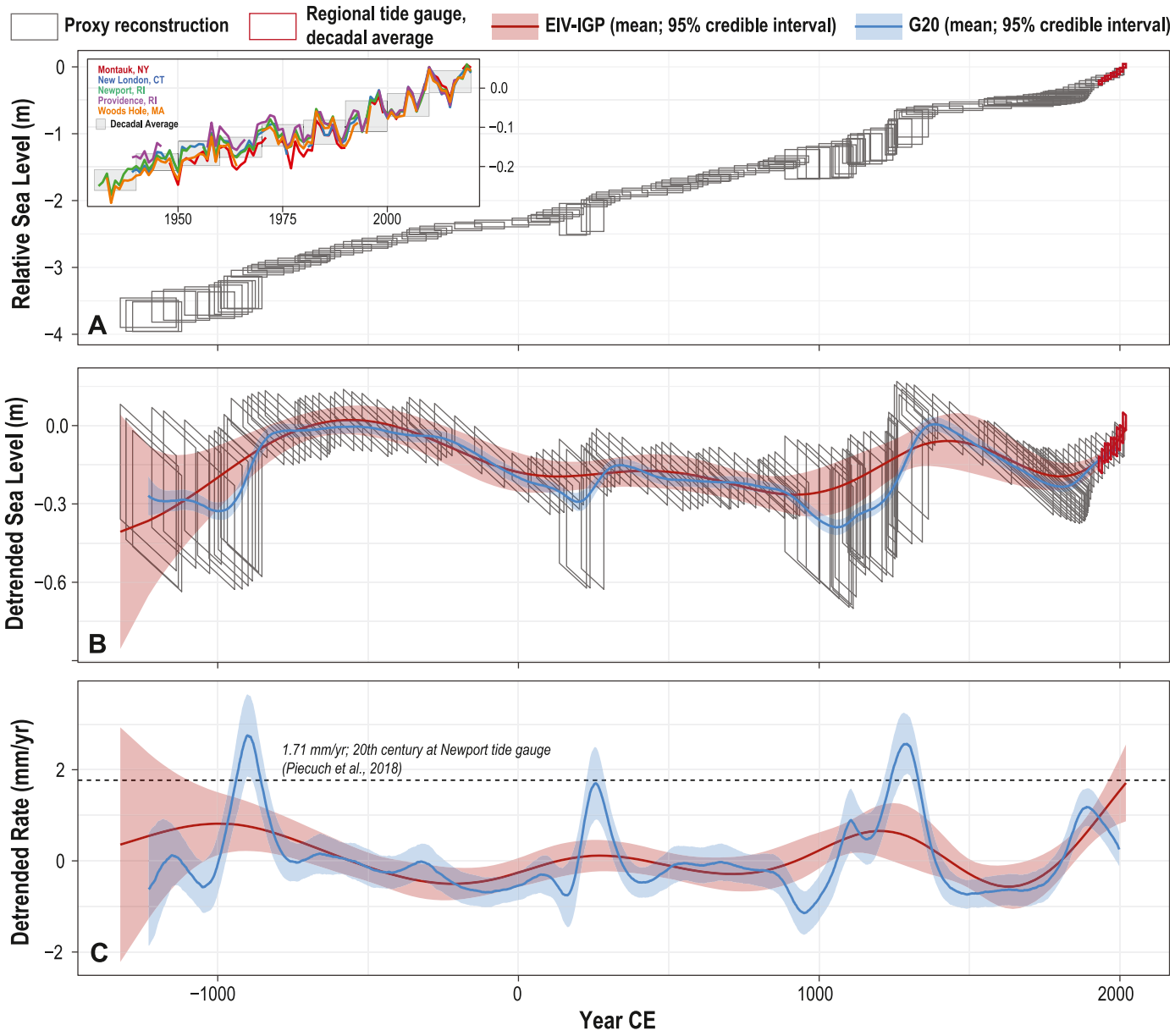

Fig. 10. Relative sea level (RSL) reconstruction for Fox Hill Marsh. **(A)** Each RSL datapoint is represented by a box which includes a 95% credible interval for sample age from the Bchron age-depth model and a 95% credible interval for vertical uncertainty from the Bayesian transfer function. Inset panel displays annual RSL measured by tide-gauges in the study region expressed relative to average RSL for 2007–2017 CE (colored lines). Boxes represent decadal average RSL measured by tide gauges and this dataset was combined with the proxy reconstruction as input for the statistical models used to quantify sea-level histories **(B)** Detrended sea level following removal of a linear trend of 1.06 mm/yr assumed to represent the contribution from ongoing glacio-isostatic adjustment (GIA). Continuous sea-level histories were generated using the errors-in-variables integrated Gaussian process (EIV-IGP) model (Cahill et al., 2015) and the statistical model utilized by Gehrels et al. (2020; G20). **(C)** Rate of detrended sea-level change estimated by the two models. Horizontal dashed line at 1.7 mm/yr represents the rate measured by the Newport tide gauge for 1930–2020 CE following correction for GIA.

scale sea-level variability (e.g., Kemp et al., 2011, 2015, Fig. 10). In contrast to the 20th century, the spatial and temporal coherence of these features (and their correlation to phases of climate variability; e.g., Kopp et al., 2016) is challenging to discern. Decomposition of pre-industrial Common Era RSL reconstructions indicates that the contribution from processes other than GIA is modest with proportionally large uncertainties (Walker et al., 2022). Before 1800 CE, global sea-level variability remained within a range of −0.2 to 0.2 mm/yr (compared to 1.3 ± 0.1 mm/yr in the 20th century in the same analysis), likely because contemporary climate forcing was also modest (PAGES2k, 2019) and lacked globally-coherent cold or warm phases (Neukom et al., 2019). Similarly, regional-scale sea-level variability on century timescales in southern New England was less than 0.3 mm/yr and at some times and places was offset by global or local-scale contributions acting in the opposite direction. For example, at Fox Hill marsh, the mean contribution to the rate of RSL change from global processes was −0.08 mm/yr (range of −0.26 to 0.14 mm/yr), compared to −0.02 mm/yr (−0.29 to 0.23 mm/yr) from regional processes, and 0.01 mm/yr (−0.4 to 0.55 mm/yr) attributed to local drivers. Given the likely scale of pre-industrial forcing and resultant sea-level variability (particularly compared to the vertical and temporal uncertainties that characterize proxy reconstructions), we propose that a relatively larger number and higher density of reconstructions is necessary to

robustly isolate contributions from global, regional, and local processes compared to efforts to identify and explain the onset of historic rise.

5.2. Influence of model choice on quantifying sea-level histories and trends

To provide an example of how the choice of statistical model may affect recognition and interpretation of sea-level trends, we analysed the Fox Hill Marsh reconstruction using two models (EIV-IGP and G20; Cahill et al., 2015; Gehrels et al., 2020) that were developed with expressly different goals. Input data followed correction for GIA and included decadal-averaged tide-gauge measurements. The EIV-IGP model generated a smooth sea-level history where rates of change are muted and sustained. Prior to the mid-19th century, mean rates of change varied from −0.56 to 0.82 mm/yr and the uncertainty in rate encompassed 0 mm/yr except for the periods previously identified. The sea-level history generated by the G20 model displays shorter-lived and larger-magnitude variability than the EIV-IGP model. Prior to the 20th century, mean rates of sea-level change range from −1.14 to 2.75 mm/yr. Notably there are two intervals (~930 BCE, and ~1300 CE) when the mean rate of change is faster than during the 20th century and a third interval (~250 CE) when the 95% credible interval includes rates in excess of those measured by nearby tide gauges. These intervals coincide with changes in PME generated by the BTF when the $\delta^{13}C_{adj}$ value of bulk sediment changed sufficiently to cause reclassification of priors indicating if a sample formed above or below MHHW. The G20 model identifies this transition to represent a large and fast RSL change, while the EIV-IGP does not. At these junctures the mid-point of consecutive RSL data points changes abruptly (although vertical uncertainties remain large relative to the change) because $\delta^{13}C_{adj}$ values are used in a discrete fashion. This change is not necessarily indicative of a large and episodic change in RSL, but rather a shift in plant community caused by a modest (few cm) change in PME. Before/after the change in $\delta^{13}C_{adj}$ values, the salt-marsh surface was narrowly below/above the MHHW threshold. This is evidenced by PME reconstructions using the BTF without informative priors (Fig. 7), which do not show rapid emergence or submergence of the salt-marsh surface since foraminiferal assemblages are largely unchanged.

Both models repeatedly sample uncertain proxy data to create an ensemble of individual sea-level trajectories that is summarized to arrive at a sea-level history. The notable differences in sea-level histories for Fox Hill Marsh generated by the two models (Fig. 10C) arise from three principal features in their architecture and choice of parameters (Cahill et al., 2015; Dangendorf, Personal Communication, 2022; Garrett et al., 2022). Firstly, the latent process quantified by the EIV-IGP model is the rate of sea-level change, which is subsequently integrated to generate sea level. A prior (−4 to 4 mm/yr for all sites) is placed on the parameter controlling variability in the rate of sea-level change. This prior reflects observed geographic variability at centennial time scales in tide-gauge records (Cahill et al., 2015). The centennial timescale approximates the amount of time represented by foraminiferal communities in sequential, 1-cm thick, slices of core sediment. The range of the prior is applicable throughout the Common Era because historic forcing was likely greater than pre-anthropogenic forcing (Neukom et al., 2019; Nidheesh et al., 2022; PAGES2k, 2019), resulting in a greater range of sea-level rates. The use of a prior means that the EIV-IGP model is unlikely to return rates of sea-level change (following correction for GIA) greater than ± 4 mm/yr. In contrast, the G20 model estimates sea-level then calculates rates of change without constraints from priors.

Secondly, the two models take different approaches to sampling the uncertain proxy data and treating temporal correlation among data points. The EIV-IGP model includes a parameter which quantifies the correlation among temporally-spaced (and stratigraphically-ordered) data points. Consequently, data points in the proxy reconstruction are not sampled individually and independently of one another, but rather entire, equi-probable trajectories are sampled. The characteristics of these sea-level rate trajectories (and hence sea-level trajectories) is dictated by the sampled covariance function at each sampling step. In the EIV-IGP model, correlation among data points declines to zero over ~1000 years on the basis that the Common Era likely includes coherent, multi-century periods of climate variability (e.g., PAGES2k, 2019). Consequently, trajectories are smooth, but non-linear, on multi-century timescales. These trajectories provide a posterior ensemble of sea-level histories conditioned on the observed data and its uncertainties. Reported results are the mean and variability across all sea-level and rate trajectories. The G20 model does not include temporal co-variance during sampling; proxy data points are sampled individually and independently to produce synthetic, error-free datapoints. After sampling, a trajectory is created by fitting a Gaussian process to the synthetic datapoints with an assumed temporal correlation structure (performed using the *fitrgp* function in MatLab). The characteristic timescale for the Gaussian process is centuries and the prior amplitude of sea-level variability is chosen for each site individually. Independently sampling datapoints with no temporal dependency structure frequently results in a synthetic sea-level dataset that includes potentially unrealistic outcomes, such as age reversals for adjacent, stratigraphically-ordered data points. These unrealistic outcomes may constitute a significant majority of trajectories given the high temporal density of datapoints. For example, in drawing downcore sample ages one million times for each of the eight proxy records shown in Fig. 11, six sites produced at least one age reversal in 100% of the iterations (at Cheesequake and Chezzetcook >81% of iterations included at least one age reversal). This result suggests that it may not be possible to generate a sea-level history that adheres to stratigraphic ordering when closely-spaced data points are sampled independently, unless the underlying probability distributions for age are distorted (e.g., forcing the deepest sample to have an age at the extreme older edge of its distribution). Importantly, the final sea-level history produced by the G20 model is generated by fitting the Gaussian process to the midpoints of the original (non-synthetic) proxy reconstruction (i.e., the temporal and vertical centre of each data point) rather than from the ensemble of trajectories, which are utilized to estimate uncertainty in the sea-level history.

Thirdly, when individual sea-level trajectories are generated, the EIV-IGP model uses a Gaussian co-variance function, which is less flexible (i.e., results in smoother sea-level trajectories) than the Matern co-variance function (smoothness factor of 3/2) utilized by the G20 model when fitting the Gaussian process. These differences between models reflect the purpose of their original development. The EIV-IGP model places greater emphasis on reconstruction uncertainties, resulting in smoother (less than ± 4 mm/yr), multi-century trends, while the G20 model was built to place greater emphasis on the mean of the underlying proxy reconstruction, resulting in trends that are more variable (in some cases reaching approximately −13 mm/yr and 10 mm/yr; Fig. 11) and shorter lived (multi-decadal to centennial).

5.3. An 18th century hotspot of sea-level rise?

Gehrels et al. (2020) proposed that a hot spot of accelerated sea-level rise occurred during the 18th century between Cape Hatteras and Nova Scotia (Fig. 1A inset). In conjunction with anti-phased

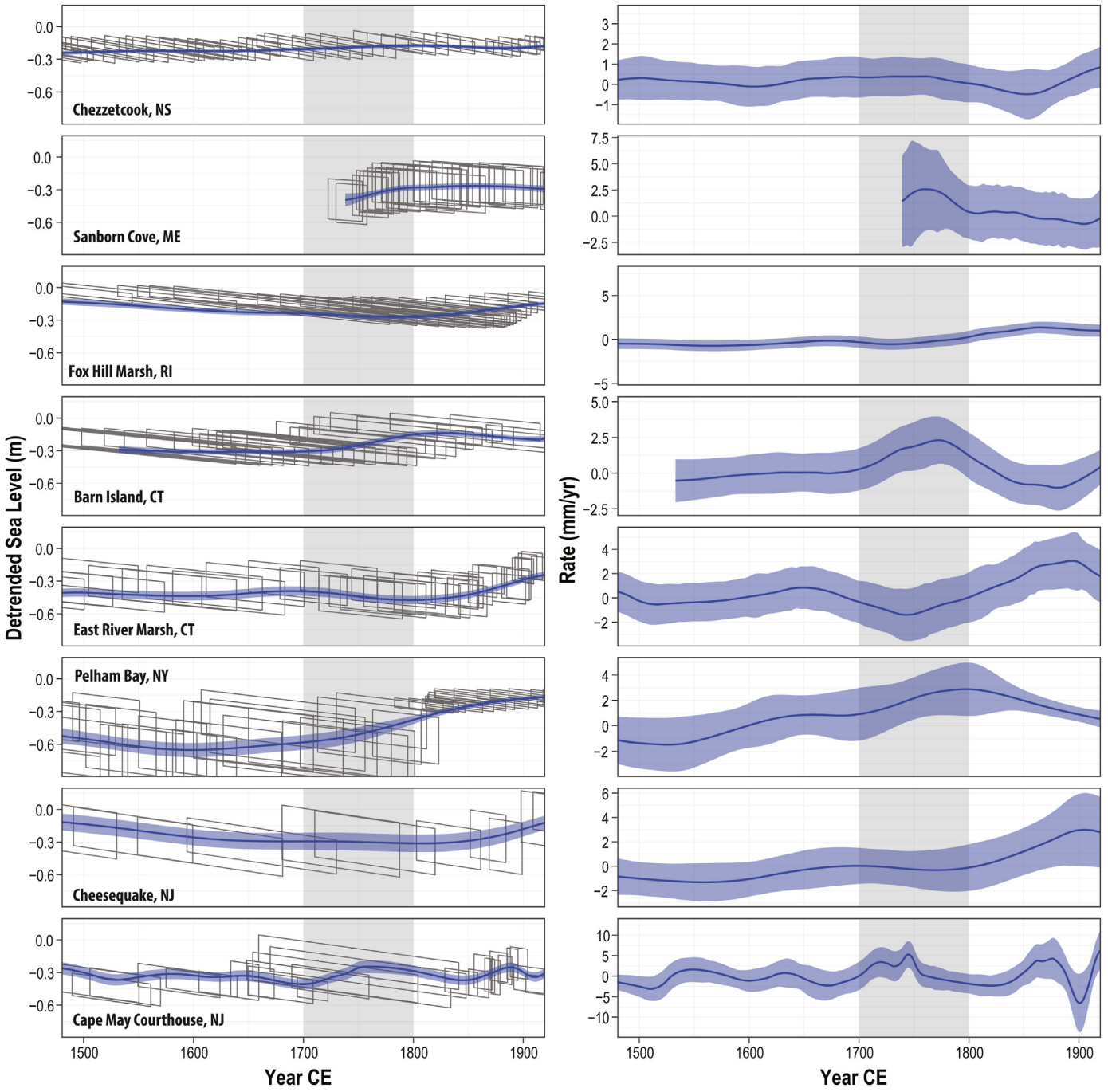

Fig. 11. Sea-level reconstructions from the proposed region that experienced an 18th century acceleration of sea-level rise. Rows represent sites organized by latitude along the Atlantic coast. Left column displays the sea-level reconstruction following correction for glacio-isostatic adjustment; each box represents sample-specific vertical and chronological uncertainties. Shaded ribbon (95% credible interval) and line are from the G20 statistical model. Axes limits are standardized across sites for ease of comparison. Right column displays the modelled rate of sea-level change from the G20 model (note that the vertical axes on the rate plots varies among panels). Shaded vertical envelope marks the 18th century.

rates of reconstructed sea-level change in Iceland, they advocated for melting of Arctic land ice as the cause of the hotspot. Given the spatial scale and extent of the proposed hotspot region, if such a period of accelerated sea-level rise occurred, it should be a feature that is widely replicated by proxy reconstructions. Using additional and updated proxy reconstructions, we re-examined the likelihood that an 18th-century hotspot of accelerated sea-level rise occurred.

We applied the G20 model (because it was intended to identify short-lived variability) to eight proxy reconstructions in the proposed hotspot region (Fig. 11). Analysis was restricted to proxy data (i.e., no tide-gauge measurements) and all estimates of GIA are from Piecuch et al. (2018b), except for Chezzetcook, Nova Scotia, which lies outside of the geographic bounds of the Piecuch et al. (2018b) analysis. A GIA rate of 1.7 mm/yr, as proposed by Gehrels et al. (2020), is used for Chezzetcook. The RSL reconstructions from Pelham Bay and East River Marsh are employed following the updates described in section 3.7. At each of the eight sites, the modelled sea-level curve lies close to the center of proxy datapoints

(see section 5.1) and comfortably within the uncertainties of the reconstructions, which are large relative to the likely magnitude of change (Fig. 11, left column). Model results from G20 do not demonstrate any spatially-coherent regional signal over the time period of approximately 1500–1900 CE. At four sites (Sanborn Cove, Barn Island, Pelham Bay, and Cape May Courthouse; Fig. 11, right column) there is an increase in the rate of rise for at least part of the 18th century, although at some of these sites the change is indistinguishable from stability within uncertainty (e.g., Sanborn Cove). At some of these sites (e.g., Pelham Bay) the increased rate of rise is part of a longer, multi-century trend, while at others (e.g., Barn Island), it is an oscillation that is completed in less than a century. Furthermore, there are pronounced differences in 18th century sea-level trends among adjacent sites. For example, the rapid rise at Barn Island (peaking in 1773 CE at 2.3 mm/yr ± 0.8 mm/yr in our emulation of G20) is located geographically (Fig. 1A) between Fox Hill Marsh (~45 km east; no apparent acceleration during 18th century) and East River Marsh (~65 km west; 18th century sea-level fall). This lack of a coherent spatial signal (even at spatial scales of 10s km) suggests that a regional-scale hotspot of rise did not occur during the 18th century, with the attendant conclusion that patterns of sea-level change are unlikely evidence for melting of land ice in the Arctic (or indeed elsewhere).

On passive margins, sea-level behavior on different temporal and spatial scales are often linked, with local-scale processes typically acting on shorter timescales than regional-scale processes (Kopp et al., 2016). Therefore, models intended to detect short-lived (sub-century) sea-level variability by emphasizing reconstruction means may identify local-scale trends that can only be meaningfully distinguished from regional-scale features where there is a high concentration (sites spaced 10s of km apart) of proxy records. The lack of a spatially-consistent hotspot of 18th century rise indicates that either a subset of sites experienced local-scale sea-level change, or that accelerated rise during the 18th century is an artifact of the underlying reconstructions. Given that the most pronounced acceleration occurs at Barn Island, in the following section we evaluate how apparent sea-level variability may arise from the underlying proxy record at this site.

5.4. Influence of reconstruction techniques and decisions

Accelerated sea-level rise is recorded in salt-marsh stratigraphies in two ways. Firstly, sedimentation rates increase in lockstep with sea-level rise and the salt-marsh surface maintains a constant tidal elevation (evidenced by stable foraminiferal assemblages and PME reconstructions). Secondly, the rate of sea-level rise exceeds the rate of sedimentation and the tidal elevation of the salt-marsh surface decreases, causing a transition in foraminiferal assemblages and lower PME reconstructions. Examination of age-depth models alongside assemblages of foraminifera and PME reconstructions provides a means to understand how these two factors influenced the identification of accelerated 18th century sea-level rise at Barn Island (Fig. 12).

The Barn Island core was dated using models of ^{210}Pb accumulation (with ^{137}Cs), recognition of the onset of industrial pollution in Pb and Cu profiles, and radiocarbon dating (Fig. 12A). The resulting age-depth model displays faster sedimentation during the 18th century (corresponding to 37–24 cm depth in the core), which contributed to the reconstructed acceleration of sea-level rise. However, the chronology of this section of the core appears problematic because the four radiocarbon ages show evidence for reversals of the age-depth relationship and possibly episodic sedimentation. This pattern continues with two depths (16 cm and 18 cm) that yielded anomalously old and reversed radiocarbon ages (these two depths were excluded from the age-depth model input by Gehrels et al., 2020). Even when presented with such reversals, age-depth models will generate an output adhering to the law of superposition (Blaauw and Heegaard, 2012; Haslett and Parnell, 2008). Other radiocarbon dated cores of salt-marsh sediment from New England (including elsewhere at Barn Island; Donnelly et al., 2004) rarely document reversals (e.g., Kemp et al., 2015; Nydick et al., 1995; van de Plassche et al., 1998; this study; Wright et al., 2017) and we propose that the frequency with which radiocarbon dates lie out of stratigraphic order at Barn Island may be evidence for disturbance. One possibility is that ditching at Barn Island during the early 20th century (Dreyer et al., 2015) physically overturned the *in-situ* salt-marsh peat captured in the core. Based on a limited stratigraphic investigation (11 cores along one, ~30-m transect) a spoil pile may have been inadvertently sampled. The uppermost part of the core retains stratigraphic ordering of samples since it accumulated after ditching, while the two lowermost radiocarbon ages (below ~45 cm) may have been below the surface onto which spoil was heaped.

Foraminifera in the Barn Island core show a notable change in assemblage at ~30 cm depth; over 50–30 cm the most abundant species is *J. macrescens*, but above 30 cm T.*inflata*/*S.lobata* and *T. comprimata* become dominant (Fig. 12B). To reconstruct PME from these assemblages, Gehrels et al. (2020) used a weighted averaging partial least squares (WA-PLS) transfer function trained on 80 modern samples from four sites. The abrupt decrease in *J. macrescens* at 30 cm caused a ~0.1 m lowering of PME (i.e., marsh drowning). Over 37–24 cm (i.e., the 18th century), PME decreased by ~0.15 m, equivalent to ~16% of great diurnal tidal range. This change contributed to the reconstruction of accelerated sea-level rise. To explore how training set composition influenced reconstructed PME, we applied a WA-PLS transfer function that used the expanded modern dataset of salt-marsh foraminifera (315 samples from 17 sites). To avoid varying the type of transfer function as well as the training set, we opted not to employ the BTF. The pattern of change in PME using this model is similar in form to Gehrels et al. (2020), but the scale of change during the 18th century is reduced by ~50%. The difference arises because near monospecific assemblages of *J. macrescens* are associated with lower elevations in the larger modern training set than they are in the data from four modern sites. We conclude that developing a transfer function using a subset (~25%) of the available modern data resulted in a PME reconstruction that shows pronounced drowning of the Barn Island salt marsh during the 18th century, which in turn generates a RSL history with rapid rise at this time.

5.5. Implications for future applications of proxy datasets to understanding late Holocene sea-level drivers

Generating proxy RSL reconstructions requires a multitude of decisions to be made from selecting a site and then a core for detailed analysis while in the field, to selecting material to date in the lab, and what type of transfer function (type and modern training data) or age-depth model to apply. Confidence in the accuracy of late Holocene RSL reconstructions (and by extension in our understanding of the processes that caused them) is strengthened when it can be demonstrated that a RSL reconstruction is not overly sensitive to decisions made in creating the record. We recommend that the robustness of proxy RSL reconstructions is tested in two ways. Firstly, a single core can be used to generate multiple RSL histories by varying the choices made during the reconstruction, such as comparing PME estimates from transfer functions trained on local and regional-scale modern training sets (e.g., Garrett et al., 2022). Secondly, generating RSL reconstructions from nearby sites where there is no *a priori* reason to expect spatial variability offers an opportunity to examine within-region

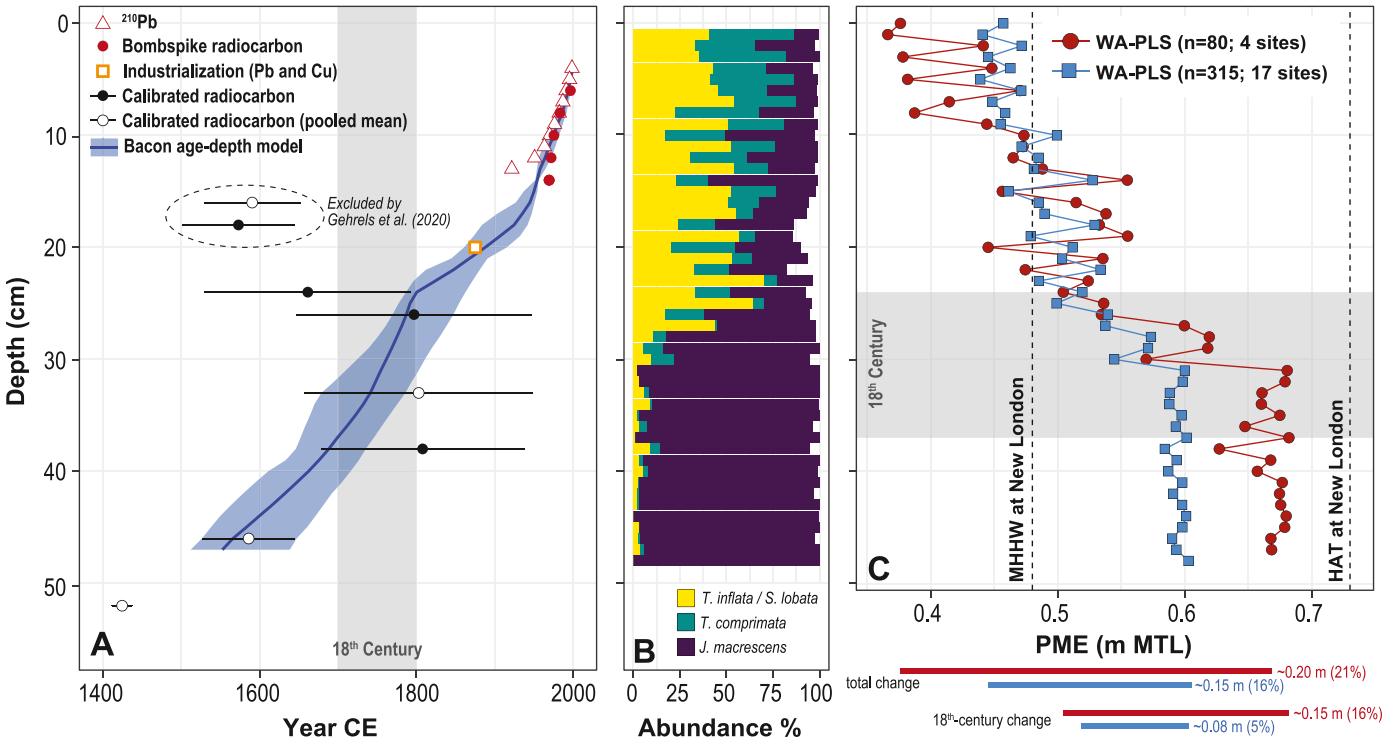

Fig. 12. Components of the relative sea-level reconstruction from Barn Island, CT (Gehrels et al., 2020). **(A)** Age-depth model. Some shallow radiocarbon dates were calibrated using the bombspike curve. Radiocarbon dates presented as pooled means represent age determinations from two or three sub samples of a single plant fragment that were combined prior to calibration. Shaded vertical envelope marks the 18th century. The age-depth model generated by Gehrels et al. (2020) is presented and excluded two dated depths (labelled) as outliers. **(B)** Relative abundance of the three most abundant taxa of foraminifera; samples below 50 cm yielded only sparse foraminifera. **(C)** Paleomarsh elevation (PME) reconstructed by weighted averaging partial least squares (WA-PLS) transfer functions trained on two modern datasets. Gehrels et al. (2020) used 80 samples from four sites and the other model utilized a dataset of 315 samples from 17 sites. The approximate change in marsh surface elevation (expressed in absolute terms and as a percentage of great diurnal tidal range; shaded bars) is presented for both models over the entire record and during the 18th century specifically. MTL = Mean Tide Level, MHHW = Mean Higher High Water, HAT = Highest Astronomical Tide

replication and to understand the spatial scales represented by any single record.

6. Conclusions

The northeastern United States and Canadian Maritimes contain the densest network of near-continuous late Holocene (last ~3000 years) RSL reconstructions and this region has been used to investigate the drivers of RSL change over this time. Yet studies invoking regional drivers of RSL change rarely evaluate if individual records (which are inherently local) or features in them identified by statistical models are reproducible among sites within a region. To address this, we reconstructed ~3000 years of RSL change at Fox Hill Marsh in Rhode Island using foraminifera and $\delta^{13}C$ signatures contained within a core of salt-marsh sediment. We constrained the chronology of the core using radiocarbon dating of plant macrofossils and recognition of pollution horizons of known age and origin. Since ~1200 BCE, RSL rose by ~3.7 m at Fox Hill Marsh. After correction for GIA, the maximum rate of rise was 1.71 ± 0.84 mm/yr (95% credible interval) in 2020 CE; a century-scale rate of rise unsurpassed in at least the previous 3000 years.

We investigated if an 18th-century hotspot of accelerated sea-level rise occurred in the northeastern United States by comparing eight proxy records from southern New Jersey to Nova Scotia. By examining an expanded and updated set of proxy RSL reconstructions, we proposed that there was not an 18th century hotspot of sea-level rise in the study region. Sites that show some evidence for faster rates of rise during the 18th century are likely influenced by local-scale factors, or reflect the impact of decisions made in generating the record. We made recommendations for future proxy-based RSL analyses that seek to identify regional trends in sea level prior to the instrumental record.

Author contributions

Rachel B. Stearns: Conceptualization, Methodology, Formal analysis, Investigation, Data curation, Writing – original draft, Writing – review & editing), Visualization. Simon E. Engelhart: Conceptualization, Methodology, Formal analysis, Investigation, Data curation, Writing – original draft, Writing – review & editing, Visualization, Supervision, Project administration, Funding acquisition. Andrew C. Kemp: Conceptualization, Methodology, Formal analysis, Data curation, Writing – original draft, Writing – review & editing, Visualization, Supervision. Troy D. Hill: Investigation, Writing – review & editing. Matthew J. Brain: Methodology, Formal analysis, Investigation, Writing – original draft, Writing – review & editing, Visualization. D. Reide Corbett: Investigation, Formal analysis, Writing – review & editing.

Declaration of competing interest

The authors declare that they have no known competing financial interests or personal relationships that could have appeared to influence the work reported in this paper.

Data availability

Data is provided in the supplementary information

Acknowledgments

Stearns was supported by a Joseph A. Cushman Award for Student Research from the Cushman Foundation for Foraminiferal Research, a Rhode Island Sea Grant award to Engelhart (2016-PD-R-1618-120-01), a National Science Foundation award to Engelhart (OCE-1458903) and by an Assistantship from the College of the Environment and Life Sciences at the University of Rhode Island. Kemp is supported by a CAREER award from the National Science Foundation (OCE-1942563) and National Science Foundation award OCE-2002431. We thank Roland Gehrels for providing us with published data from Barn Island, Niamh Cahill and Soenke Dangendorf for extensive conversations about the structure and implementation of the EIV-IGP and G20 models, respectively, Jennifer Walker for providing model results, and the Earthwatch IGNITE program through which 40 IGNITE high school students assisted with data collection across field seasons in 2015–2019 along with Jason Padgett, Matt Gerlach, Byron Halavik, Greta Janigian, Dan Russell, Caroline Amelse, Tim Shaw, and Jennifer Walker. Views expressed in this article are those of the authors and do not necessarily represent the views or policies of the U.S. Environmental Protection Agency or National Park Service. Use of trade, firm, or product names does not imply endorsement by the U.S. Government. Two anonymous reviewers provided constructive and detailed comments during the review process, and we are grateful for this assistance. This paper is a contribution to IGCP Project 639 “Sea-Level Changes from Minutes to Millennia” and IGCP Project 725 “Forecasting Coastal Change”.

Appendix A. Supplementary data

Supplementary data to this article can be found online at https://doi.org/10.1016/j.quascirev.2022.107868.

References

Akpati, B.N., 1975. Foraminiferal distribution and environmental variables in eastern Long Island Sound, New York. J. Foraminifer. Res. 5, 127–144.
Ashe, E.L., Cahill, N., Hay, C., Khan, N.S., Kemp, A.C., Engelhart, S.E., Horton, B.P., Parnell, A.C., Kopp, R.E., 2019. Statistical modeling of rates and trends in Holocene relative sea level. Quat. Sci. Rev. 204, 58–77.
Barlow, N.L.M., Shennan, I., Long, A.J., Gehrels, W.R., Saher, M.H., Woodroffe, S.A., Hillier, C., 2013. Salt marshes as late Holocene tide gauges. Global Planet. Change 106, 90–110.
Barnett, R.L., Bernatchez, P., Garneau, M., Brain, M.J., Charman, D.J., Stephenson, D.B., Haley, S., Sanderson, N., 2019. Late Holocene sea-level changes in eastern Québec and potential drivers. Quat. Sci. Rev. 203, 151–169.
Barnett, R.L., Bernatchez, P., Garneau, M., Juneau, M.N., 2017. Reconstructing late Holocene relative sea-level changes at the Magdalen Islands (Gulf of St. Lawrence, Canada) using multi-proxy analyses. J. Quat. Sci. 32, 380–395.
Benner, R., Fogel, M.L., Sprague, E.K., Hodson, R.E., 1987. Depletion of ^{13}C in lignin and its implications for stable isotope studies. Nature 329, 708–710.
Bertness, M.D., 1991. Zonation of *Spartina patens* and *Spartina alterniflora* in new England salt marsh. Ecology 72, 138–148.
Bittermann, K., Rahmstorf, S., Perrette, M., Vermeer, M., 2013. Predictability of twentieth century sea-level rise from past data. Environ. Res. Lett. 8, 014013.
Blaauw, M., Heegaard, E., 2012. Estimation of age-depth relationships. In: Birks, H.J.B., Lotter, A.F., Juggins, S., Smol, J.P. (Eds.), Tracking Environmental Change Using Lake Sediments. Springer Netherlands, pp. 379–413.
Bloom, A.L., 1964. Peat accumulation and compaction in Connecticut coastal marsh. J. Sediment. Res. 34, 599–603.
Bollhöfer, A., Rosman, K.J.R., 2001. Isotopic source signatures for atmospheric lead: the Northern Hemisphere. Geochem. Cosmochim. Acta 65, 1727–1740.
Brain, M.J., 2016. Past, present and future perspectives of sediment compaction as a driver of relative sea level and coastal change. Curr. Clim. Change Rep. 2, 75–85.
Brain, M.J., Kemp, A.C., Hawkes, A.D., Vane, C.H., Cahill, N., Hill, T.D., Engelhart, S.E., Donnelly, J.P., Horton, B.P., 2017. The contribution of mechanical compression and biodegradation to compaction of salt-marsh sediments and relative sea-level reconstructions. Quat. Sci. Rev. 167, 96–111.
Brain, M.J., Kemp, A.C., Horton, B.P., Culver, S.J., Parnell, A.C., Cahill, N., 2015. Quantifying the contribution of sediment compaction to late Holocene salt-marsh sea-level reconstructions, North Carolina, USA. Quat. Res. 83, 41–51.
Brain, M.J., Long, A.J., Petley, D.N., Horton, B.P., Allison, R.J., 2011. Compression behaviour of minerogenic low energy intertidal sediments. Sediment. Geol. 233, 28–41.
Brain, M.J., Long, A.J., Woodroffe, S.A., Petley, D.N., Milledge, D.G., Parnell, A.C., 2012. Modelling the effects of sediment compaction on salt marsh reconstructions of recent sea-level rise. Earth Planet Sci. Lett. 345–348, 180–193.
Bricker-Urso, S., Nixon, S.W., Cochran, J.K., Hirschberg, D.J., Hunt, C., 1989. Accretion rates and sediment accumulation in Rhode Island salt marshes. Estuaries 12, 300–317.
Buzas, M.A., 1965. The Distribution and Abundance of Foraminifera in Long Island Sound. Smithsonian Miscellaneous Collections.
Cahill, N., Kemp, A.C., Horton, B.P., Parnell, A.C., 2015. Modeling sea-level change using errors-in-variables intergrated Gaussian processes. Ann. Appl. Stat. 9, 547–571.
Cahill, N., Kemp, A.C., Parnell, A.C., Horton, B.P., 2016. A Bayesian hierarchical model for reconstructing relative sea level: from raw data to rates. Clim. Past 12, 525–542.
Chmura, G.L., Aharon, P., 1995. Stable carbon isotope signatures of sedimentary carbon in coastal wetlands as indicators of salinity regime. J. Coast Res. 11, 124–135.
Chmura, G.L., Aharon, P., Socki, R.A., Abernethy, R., 1987. An inventory of ^{13}C abundances in coastal wetlands of Louisiana, USA: vegetation and sediments. Oecologia 74, 264–271.
Choi, Y., Wang, Y., Hsieh, Y.P., Robinson, L., 2001. Vegetation succession and carbon sequestration in a coastal wetland in northwest Florida: evidence from carbon isotopes. Global Biogeochem. Cycles 15, 311–319.
Church, John, White, Neil, 2011. Sea-Level Rise from the Late 19th to the Early 21st Century. Surveys in Geophysics 32, 585–602. https://doi.org/10.1007/s10712-011-9119-1.
Clark, J.A., Farrell, W.E., Peltier, W.R., 1978. Global changes in postglacial sea level: a numerical calculation. Quat. Res. 9, 265–287.
Corbett, D.R., Walsh, J.P., 2015. ^{210}Lead and ^{137}Cesium: establishing a chronology for the last century. In: Shennan, I., Long, A.J., Horton, B.P. (Eds.), Handbook of Sea Level Research. John Wiley & Sons, Chichester, pp. 361–372.
Crain, C.M., Albertson, L.K., Bertness, M.D., 2008. Secondary succession dynamics in estuarine marshes across landscape-scale salinity gradients. Ecology 89, 2889–2899.
Donnelly, J.P., 2006. A revised late Holocene sea-level record for northern Massachusetts, USA. J. Coast Res. 22, 1051–1061.
Donnelly, J.P., Bertness, M.D., 2001. Rapid shoreward encroachment of salt marsh cordgrass in response to accelerated sea-level rise. Proc. Natl. Acad. Sci. U. S. A 98, 14218–14223.
Donnelly, J.P., Cleary, P., Newby, P., Ettinger, R., 2004. Coupling instrumental and geological records of sea-level change: evidence from southern New England of an increase in the rate of sea-level rise in the late 19th century. Geophys. Res. Lett. 31, L05203.
Dreyer, G., Rozsa, R., Jones, C., 2015. Management Assessment Report Barn Island Wildlife Management Area Stonington. Connecticut College Arboretum, Connecticut, p. 73.
Dunnington, D.W., Roberts, S., Norton, S.A., Spooner, I.S., Kurek, J., Kirk, J.L., Muir, D.C.G., White, C.E., Gagnon, G.A., 2020. The distribution and transport of lead over two centuries as recorded by lake sediments from northeastern North America. Sci. Total Environ. 737, 140212.
Edwards, R.J., Wright, A.J., 2015. Foraminifera. In: Shennan, I., Long, A.J., Horton, B.P. (Eds.), Handbook of Sea-Level Research. John Wiley & Sons, Chichester, pp. 191–217.
Edwards, R.J., Wright, A.J., van de Plassche, O., 2004. Surface distributions of salt-marsh foraminifera from Connecticut, USA: modern analogues for high-resolution sea level studies. Mar. Micropaleontol. 51, 1–21.
Engelhart, S.E., Horton, B.P., 2012. Holocene sea level database for the Atlantic coast of the United States. Quat. Sci. Rev. 54, 12–25.
Engelhart, S.E., Horton, B.P., Douglas, B.C., Peltier, W.R., Tornqvist, T.E., 2009. Spatial variability of late Holocene and 20th century sea-level rise along the Atlantic coast of the United States. Geology 37, 1115–1118.
Filipescu, S., Kaminski, M.A., 2011. Re-discovering *Entzia*, an agglutinated foraminer from the Transylvanian salt marshes. In: Kaminski, M.A., Filipescu, S. (Eds.), Proceedings of the Eight International Workshop on Agglutinated Foraminfera, vol. 16. Grzybowski Foundation Special Publication, pp. 29–35.
Francey, R., Allison, C., Etheridge, D., Trudinger, C., Enting, I., Leuenberger, M., Langenfelds, R., Michel, E., Steele, L., 1999. A 1000-year high precision record of δ13C in atmospheric CO2. Tellus B 51, 170–193.
Frederikse, T., Landerer, F., Caron, L., Adhikari, S., Parkes, D., Humphrey, V.W., Dangendorf, S., Hogarth, P., Zanna, L., Cheng, L., Wu, Y.-H., 2020. The causes of sea-level rise since 1900. Nature 584, 393.
Garrett, E., Gehrels, W.R., Hayward, B.W., Newnham, R., Gehrels, M.J., Morey, C.J., Dangendorf, S., 2022. Drivers of 20th century sea-level change in southern New Zealand determined from proxy and instrumental records. Journal of Quaternary Science n/a.
Gebrehiwet, T., Koretsky, C.M., Krishnamurthy, R.V., 2008. Influence of *Spartina* and *Juncus* on saltmarsh sediments III; organic geochemistry. Chem. Geol. 255, 114–119.
Gehrels, W.R., Dangendorf, S., Barlow, N., Saher, M., Long, A., Woodworth, P., Piecuch, C., Berk, K., 2020. A preindustrial sea-level rise hotspot along the Atlantic coast of North America. Geophys. Res. Lett. 47, e2019GL085814.
Gehrels, W.R., Dawson, D.A., Shaw, J., Marshall, W.A., 2011. Using Holocene relative sea-level data to inform future sea-level predictions: an example from south-west England. Global Planet. Change 78, 116–126.

Gehrels, W.R., Kirby, J.R., Prokoph, A., Newnham, R.M., Achterberg, E.P., Evans, H., Black, S., Scott, D.B., 2005. Onset of recent rapid sea-level rise in the western Atlantic Ocean. Quat. Sci. Rev. 24, 2083–2100.
Gehrels, W.R., van de Plassche, O., 1999. The use of *Jadammina macrescens* (brady) and *Balticammina pseudomacrescens* Brönnimann, Lutze and Whittaker (Protozoa: Foraminiferida) as Sea-level indicators. Palaeogeogr. Palaeoclimatol. Palaeoecol. 149, 89–101.
Gerlach, M.J., Engelhart, S.E., Kemp, A.C., Moyer, R.P., Smoak, J.M., Bernhardt, C.E., Cahill, N., 2017. Reconstructing Common Era relative sea-level change on the Gulf coast of Florida. Mar. Geol. 390, 254–269.
Gobeil, C., Tessier, A., Couture, R.-M., 2013. Upper Mississippi Pb as a mid-1800s chronostratigraphic marker in sediments from seasonally anoxic lakes in Eastern Canada. Geochem. Cosmochim. Acta 113, 125–135.
Haslett, J., Parnell, A., 2008. A simple monotone process with application to radiocarbon-dated depth chronologies. J. Roy. Stat. Soc.: Series C (Applied Statistics) 57, 399–418.
Hay, Carling, Morrow, Eric, Kopp, Robert, Mitrovica, Jerry, 2015. Probabilistic reanalysis of twentieth-century sea-level rise. Nature 517, 481–484. https://doi.org/10.1038/nature14093.
Hobbs, N.B., 1986. Mire morphology and the properties and behaviour of some British and foreign peats. Q. J. Eng. Geol. Hydrogeol. 19, 7–80.
Horton, B.P., 1999. The contemporary distribution of intertidal foraminifera of Cowpen Marsh, Tees Estuary, UK: implications for studies of Holocene sea-level changes. Palaeogeography, Palaeoclimatology, Palaeoecology, Special Issue 149, 127–149.
Hurst, R.W., 2000. Applications of anthropogenic lead archaeostratigraphy (ALAS model) to hydrocarbon remediation. Environ. Forensics 1, 11–23.
Johnson, B.J., Moore, K.A., Lehmann, C., Bohlen, C., Brown, T.A., 2007. Middle to late Holocene fluctuations of C_3 and C_4 vegetation in a northern new England salt marsh, Sprague marsh, Phippsburg Maine. Org. Geochem. 38, 394–403.
Johnson, D.S., York, H.H., 1915. The Relation of Plants to Tide-Levels; a Study of Factors Affecting the Distribution of Marine Plants. Carnegie Institution of Washington, Washington, D.C.
Karegar, M.A., Dixon, T.H., Engelhart, S.E., 2016. Subsidence along the Atlantic coast of North America: insights from GPS and late Holocene relative sea level data. Geophys. Res. Lett. 43, 3126–3133.
Keeling, C.D., 1979. The Suess effect: ^{13}Carbon-^{14}Carbon interrelations. Environ. Int. 2, 229–300.
Keeling, C.D., Piper, S.C., Bacastow, R.B., Wahlen, M., Whorf, T.P., Heimann, M., Meijer, H.A., 2001. Exchanges of Atmospheric CO_2 and $^{13}CO_2$ with the Terrestrial Biosphere and Oceans from 1978 to 2000. I. Global Aspects, Scripps Institution of Oceanography Reference Series. Scripps Institution of Oceanography, p. 88.
Kemp, A.C., Cahill, N., Engelhart, S.E., Hawkes, A.D., Wang, K., 2018a. Revising estimates of spatially variable subsidence during the A.D. 1700 Cascadia earthquake using a Bayesian foraminiferal transfer function. Bull. Seismol. Soc. Am. 108, 654–673.
Kemp, A.C., Hawkes, A.D., Donnelly, J.P., Vane, C.H., Horton, B.P., Hill, T.D., Anisfeld, S.C., Parnell, A.C., Cahill, N., 2015. Relative sea-level change in Connecticut (USA) during the last 2200 years. Earth Planet Sci. Lett. 428, 217–229.
Kemp, A.C., Hill, T.D., Vane, C.H., Cahill, N., Orton, P., Talke, S.A., Parnell, A.C., Sanborn, K., Hartig, E.K., 2017a. Relative sea-level trends in New York City during the past 1500 years. Holocene 27, 1169–1186.
Kemp, A.C., Horton, B., Donnelly, J.P., Mann, M.E., Vermeer, M., Rahmstorf, S., 2011. Climate related sea-level variations over the past two millennia. Proc. Natl. Acad. Sci. USA 108, 11017–11022.
Kemp, A.C., Horton, B.P., Vane, C.H., Corbett, D.R., Bernhardt, C.E., Engelhart, S.E., Anisfeld, S.C., Parnell, A.C., Cahill, N., 2013a. Sea-level change during the last 2500 years in New Jersey, USA. Quat. Sci. Rev. 81, 90–104.
Kemp, A.C., Kegel, J.J., Culver, S.J., Barber, D.C., Mallinson, D.J., Leorri, E., Bernhardt, C.E., Cahill, N., Riggs, S.R., Woodson, A.L., Mulligan, R.P., Horton, B.P., 2017b. Extended late Holocene relative sea-level histories for North Carolina, USA. Quat. Sci. Rev. 160, 13–30.
Kemp, A.C., Nelson, A.R., Horton, B.P., 2013b. Radiocarbon dating of plant macrofossils in tidal marsh sediment. In: Schroder, J. (Ed.), Treatise on Geomorphology. Academic Press, San Diego, CA, pp. 370–388.
Kemp, A.C., Sommerfield, C.K., Vane, C.H., Horton, B.P., Chenery, S.R., Anisfeld, S.C., Nikitina, D., 2012a. Use of lead isotopes for developing chronologies in recent salt-marsh sediments. Quat. Geochronol. 12, 40–49.
Kemp, A.C., Telford, R.J., 2015. Transfer functions. In: Shennan, I., Long, A.J., Horton, B.P. (Eds.), Handbook for Sea-Level Research. John Wiley & Sons, Chichester, pp. 470–499.
Kemp, A.C., Vane, C.H., Horton, B.P., Culver, S.J., 2010. Stable carbon isotopes as potential sea-level indicators in salt marshes, North Carolina, USA. Holocene 20, 623–636.
Kemp, A.C., Vane, C.H., Horton, B.P., Engelhart, S.E., Nikitina, D., 2012b. Application of stable carbon isotopes for reconstructing salt-marsh floral zones and relative sea level, New Jersey, USA. J. Quat. Sci. 27, 404–414.
Kemp, A.C., Wright, A.J., Cahill, N., 2020. Enough is enough, or more is more? Testing the influence of foraminiferal count size on reconstructions of paleo-marsh elevation. J. Foraminifer. Res. 50, 266–278.
Kemp, A.C., Wright, A.J., Edwards, R.J.B., Brain, R.L., Cahill, N., Kopp, R.E., Horton, B.P., Charman, D.J., Hawkes, A.D., Hill, T.D., van de Plassche, O., 2018b. Relative sea-level change in Newfoundland, Canada during the past ~3000 years. M. Quat. Sci. Rev. 201, 89–110.
Kopp, R.E., Kemp, A.C., Bitterman, K., Horton, B.P., Donnelly, J.P., Gehrels, W.R., Hay, C., Mitrovica, J.X., Morrow, E., Rahmstorf, S., 2016. Temperature-driven global sea-level variability in the Common Era. Proc. Natl. Acad. Sci. USA 113, E1434–E1441.
Lamb, A.L., Wilson, G.P., Leng, M.J., 2006. A review of coastal palaeoclimate and relative sea-level reconstructions using δ^{13}C and C/N ratios in organic material. Earth Sci. Rev. 75, 29–57.
Lima, A.L., Bergquist, B.A., Boyle, E.A., Reuer, M.K., Dudas, F.O., Reddy, C.M., Eglinton, T.I., 2005. High-resolution historical records from Pettaquamscutt River basin sediments: 2. Pb isotopes reveal a potential new stratigraphic marker. Geochem. Cosmochim. Acta 69, 1813–1824.
Linsley, B.K., Dunbar, R.B., Dassié, E.P., Tangri, N., Wu, H.C., Brenner, L.D., Wellington, G.M., 2019. Coral carbon isotope sensitivity to growth rate and water depth with paleo-sea level implications. Nat. Commun. 10, 2056.
Long, A.J., Waller, M.P., Stupples, P., 2006. Driving mechanisms of coastal change: peat compaction and the destruction of late Holocene coastal wetlands. Mar. Geol. 225, 63–84.
McCarthy, G.D., Haigh, I.D., Hirschi, J.J.M., Grist, J.P., Smeed, D.A., 2015. Ocean impact on decadal Atlantic climate variability revealed by sea-level observations. Nature 521, 508–510.
Middleburg, J.J., Nieuwenhuize, J., Lubberts, R.K., van de Plassche, O., 1997. Organic carbon isotope systematics of coastal marshes. Estuar. Coast Shelf Sci. 45, 681–687.
Milne, G.A., Gehrels, W.R., Hughes, C.W., Tamisiea, M.E., 2009. Identifying the causes of sea-level change. Nat. Geosci. 2, 471–478.
Neukom, R., Steiger, N., Gómez-Navarro, J.J., Wang, J., Werner, J.P., 2019. No evidence for globally coherent warm and cold periods over the preindustrial Common Era. Nature 571, 550–554.
Nidheesh, G., Goosse, H., Parkes, D., Goelzer, H., Maussion, F., Marzeion, B., 2022. Process-based estimate of global-mean sea-level changes in the Common Era. Earth Syst. Dynam. Discuss. 2022, 1–31.
Niering, W.A., Warren, R.S., 1980. Vegetation patterns and processes in new England salt marshes. Bioscience 30, 301–307.
Niering, W.A., Warren, R.S., Weymouth, C.G., 1977. Our Dynamic Tidal Marshes: Vegetation Changes as Revealed by Peat Analysis, 22 ed. The Connecticut Arboretum Bulletin, p. 12.
Nixon, S.W., 1982. The Ecology of New England High Salt Marshes: a Community Profile. Fish and Wildlife Service. US Department of the Interior.
Nydick, K.R., Bidwell, A.B., Thomas, E., Varekamp, J.C., 1995. A sea-level rise curve from Guilford, Connecticut, USA. Mar. Geol. 124, 137–159.
Oakley, B.A., Boothroyd, J.C., 2013. Constrained age of glacial lake Narragansett and the deglacial chronology of the Laurentide ice Sheet in southeastern new England. J. Paleolimnol. 50, 305–317.
PAGES2k, C., 2019. Consistent multidecadal variability in global temperature reconstructions and simulations over the Common Era. Nat. Geosci. 12, 643–649.
Parnell, A.C., Buck, C.E., Doan, T.K., 2011. A review of statistical chronology models for high-resolution, proxy-based Holocene palaeoenvironmental reconstruction. Quat. Sci. Rev. 30, 2948–2960.
Parnell, A.C., Gehrels, W.R., 2015. Using chronological models in late Holocene sea-level reconstructions from saltmarsh sediments. In: Shennan, I., Long, A.J., Horton, B.P. (Eds.), Handbook of Sea-Level Research. John Wiley & Sons, pp. 500–513.
Parnell, A.C., Haslett, J., Allen, J.R.M., Buck, C.E., Huntley, B., 2008. A flexible approach to assessing synchroneity of past events using Bayesian reconstructions of sedimentation history. Quat. Sci. Rev. 27, 1872–1885.
Peck, J.A., McMaster, R.L., 1991. Stratigraphy and geologic history of quaternary sediments in lower west passage, Narragansett bay, Rhode Island. J. Coast Res. 25–37.
Peltier, W.R., 1996. Global sea level rise and glacial isostatic adjustment: an analysis of data from the east coast of North America. Geophys. Res. Lett. 23, GL00848.
Peltier, W.R., Argus, D.F., Drummond, R., 2015. Space geodesy constrains ice-age terminal deglaciation: the ICE-6G_C (VM5a) model. J. Geophys. Res. Solid Earth 120, 450–487.
Peteet, D.M., Nichols, J., Kenna, T., Chang, C., Browne, J., Reza, M., Kovari, S., Liberman, L., Stern-Protz, S., 2018. Sediment starvation destroys New York City marshes' resistance to sea level rise. Proc. Natl. Acad. Sci. USA.
Piecuch, C.G., Bittermann, K., Kemp, A.C., Ponte, R.M., Little, C.M., Engelhart, S.E., Lentz, S.J., 2018a. River-discharge effects on United States Atlantic and Gulf coast sea-level changes. Proc. Natl. Acad. Sci. USA 115, 7729–7734.
Piecuch, C.G., Dangendorf, S., Ponte, R.M., Marcos, M., 2016. Annual sea level changes on the North American northeast coast: influence of local winds and barotropic motions. J. Clim. 29, 4801–4816.
Piecuch, C.G., Huybers, P., Hay, C.C., Kemp, A.C., Little, C.M., Mitrovica, J.X., Ponte, R.M., Tingley, M.P., 2018b. Origin of spatial variation in US East Coast sea-level trends during 1900–2017. Nature 564, 400–404.
Redfield, A.C., 1972. Development of a new England salt marsh. Ecol. Monogr. 42, 201–237.
Reimer, P.J., Austin, W.E., Bard, E., Bayliss, A., Blackwell, P.G., Ramsey, C.B., Butzin, M., Cheng, H., Edwards, R.L., Friedrich, M., 2020. The IntCal20 Northern Hemisphere radiocarbon age calibration curve (0–55 cal kBP). Radiocarbon 62, 725–757.
Schonfeld, J., Mendes, I., 2022. Benthic foraminifera and pore water carbonate chemistry on a tidal flat and salt marsh at Ria Formose, Algarve, Portugal. Estuarine. Coastal and Shelf Science 276, 108003.
Scott, D.B., Hermelin, J.O.R., 1993. A device for precision splitting of micropaleontological samples in liquid suspension. J. Paleontol. 67, 151–154.
Scott, D.B., Medioli, F.S., 1978. Vertical zonations of marsh foraminifera as accurate

indicators of former sea levels. Nature 272, 528–531.
Scott, D.B., Medioli, F.S., 1980. Living vs. Total foraminiferal populations: their relative usefulness in Paleoecology. J. Paleontol. 54 (4), 814–831.
Shennan, I., Horton, B., 2002. Holocene land- and sea-level changes in Great Britain. J. Quat. Sci. 17, 511–526.
Simpson, G.L., 2007. Analogue methods in Palaeoecology: using the analogue package. J. Stat. Software 22, 1–29.
Simpson, G.L., 2012. Analogue methods. In: Birks, H.J.B., Lotter, A.F., Juggins, S., Smol, J.P. (Eds.), Data Handling and Numerical Techniques. Springer, Dordrecht, pp. 495–522.
Strauss, B.H., Ziemlinski, R., Weiss, J.L., Overpeck, J.T., 2012. Tidally adjusted estimates of topographic vulnerability to sea level rise and flooding for the contiguous United States. Environ. Res. Lett. 7, 014033.
Tanner, B.R., Uhle, M.E., Mora, C.I., Kelley, J.T., Schuneman, P.J., Lane, C.S., Allen, E.S., 2010. Comparison of bulk and compound-specific $\delta^{13}C$ analyses and determination of carbon sources to salt marsh sediments using n-alkane distributions (Maine, USA). Estuar. Coast Shelf Sci. 86, 283–291.
Thomas, E., Gapotchenko, T., Varekamp, J.C., Mecray, E.L., Brink, M.R.B.t., 2000. Benthic foraminifera and environmental changes in long island Sound. J. Coast Res. 16, 641–655.
Troels-Smith, J., 1955. Karakterising af lose jordater. Danmarks Geologiske Undersogelse 3, 39–73.
van de Plassche, O., van der Borg, K., de Jong, A.F.M., 1998. Sea level-climate correlation during the past 1400 yr. Geology 26, 319–322.
Varekamp, J., Kreulen, B., ten Brink, B.M., Mecray, E., 2003. Mercury contamination chronologies from Connecticut wetlands and Long Island Sound sediments. Environ. Geol. 43, 268–282.
Walker, J.S., Kopp, R.E., Shaw, T.A., Cahill, N., Khan, N.S., Barber, D.C., Ashe, E.L., Brain, M.J., Clear, J.L., Corbett, D.R., Horton, B.P., 2021. Common Era sea-level budgets along the U.S. Atlantic coast. Nat. Commun. 12, 1841.
Walker, J.S., Kopp, R.E., Little, C.M., Horton, B.P., 2022. Timing of emergence of modern rates of sea-level rise by 1863. Nat. Commun. 13, 966.
Walton, W.R., 1952. Techniques for Recognition of Living Foraminifera, vol. 3. Cushman Foundation for Foraminiferal Research, pp. 56–60.
Wigand, C., McKinney, R.A., Charpentier, M.A., Chintala, M.M., Thursby, G.B., 2003. Relationships of nitrogen loadings, residential development, and physical characteristics with plant structure in New England salt marshes. Estuaries 26, 1494–1504.
Wilson, G.P., 2017. On the application of contemporary bulk sediment organic carbon isotope and geochemical datasets for Holocene sea-level reconstruction in NW Europe. Geochem. Cosmochim. Acta 214, 191–208.
Wozniak, A.S., Roman, C.T., Wainright, S.C., McKinney, R.A., James-Pirri, M.-J., 2006. Monitoring food web changes in tide-restored salt marshes: a carbon stable isotope approach. Estuar. Coast 29, 568–578.
Wright, A.J., Edwards, R.J., van de Plassche, O., 2011. Reassessing transfer-function performance in sea-level reconstruction based on benthic salt-marsh foraminifera from the Atlantic coast of NE North America. Mar. Micropaleontol. 81, 43–62.
Wright, A.J., Edwards, R.J., van de Plassche, O., Blaauw, M., Parnell, A.C., van der Borg, K., de Jong, A.F., Roe, H.M., Selby, K., Black, S., 2017. Reconstructing the accumulation history of a saltmarsh sediment core: which age-depth model is best? Quat. Geochronol. 39, 35–67.